UNIVERSIDAD NACIONAL AUTÓNOMA DE MÉXICO

FACULTAD DE CIENCIAS

MONTE CARLO SIMULATIONS FOR A TONNE-SCALE BUBBLE CHAMBER TO SEARCH FOR DARK MATTER

T E S I S

QUE PARA OBTENER EL TÍTULO DE:

LICENCIADO EN FÍSICA

P R E S E N T A :

ENRIQUETA NORIEGA BENÍTEZ

TUTOR

DR. ERIC VÁZQUEZ JÁUREGUI

MÉXICO, CDMX, 2019.

Hoja de Datos del Jurado

1. Datos del alumno
   Noriega
   Benítez
   Enriqueta
   5527087867
   Universidad Nacional Autónoma de México
   Facultad de Ciencias
   Física
   312515892
2. Datos del tutor
   Dr.
   Eric
   Vázuqez
   Jáuregui
3. Datos del sinodal 1
   Dr.
   Juan Carlos
   D'Olivo
   Saez
4. Datos del sinodal 2
   Dra.
   Gabriela
   Murguía
   Romero
5. Datos del sinodal 3
   Dra.
   Libertad
   Barrón
   Palos
6. Datos del sinodal 4
   Dr.
   Eduardo
   Peinado
   Rodriguez
7. Datos del trabajo escrito
   Monte Carlo Simulations for a Tonne-Scale Bubble Chamber to Search for
   Dark Matter
   69 pp
   2019

To mum and dad...

Contents

List of Figures

Introduction

Through different studies it has become clear that there are several hints that tell us that our knowledge of the Universe is still limited. There are sundry observations that demand clearer and complex explanations. It appears that there is a large amount of data that suggests a large portion of the Universe's content is made of non-luminous matter. These indicators in astrophysical and cosmological results, such as rotational curves of galaxies and anisotropies of the cosmic microwave background, advocate for the existence of dark matter. According to this approach, dark matter would embody $22.7 \pm 1.4\%$ of the Universe [3].

This theory is not new, its first mention was in the early 1930's when Zwicky observed that the movement of galaxies did not resemble the expected motion as the Coma cluster seemed to move too rapidly in his examination. The galaxy was moving too fast and the gravitational attraction of the visible matter was not sufficient to clasp it [4]. Therefore, a big extra amount of matter was to be disregarded and an explanation for the missing matter was called for. The idea of dark matter, introduced as extra unseen matter, was considered to explain the gravitational force driving the galaxy's acceleration.

Dark matter theory popularity has increased throughout the years. The idea that there exists matter that does not emit electromagnetic radiation is compatible with different kinds of measurements; gravitational lenses and x-ray radiation of galaxy clusters, CMB and the abundance of light elements. With increasing consideration, the theory changes were unavoidable and questions concerning its nature arose. When did it originate? Is it stable? Why haven't we previously detected such particles? Cosmology and particle physics are deeply immersed in trying to find dark matter. There are several efforts worldwide trying to detect dark matter interactions with ordinary matter: spatial modules, NaI crystals in the Antarctic, particle accelerators and particle detectors. One of these attempts is being carried out in Sudbury, Canada. SNOLAB is a facility located 2 km underground, and it's home to several experiments. Particularly, PICO, is a collaboration in which bubble chamber technology is studied and developed. PICO's purpose is to prove the existence of one of the strongest candidates for dark matter: the WIMP (Weakly Interacting Massive Particles). This attractive candidate introduces a new exotic particle with a host of properties such as being electrically neutral, non-relativistic, non-baryonic and that must interact weakly with ordinary matter. Dark matter candidates' theory frame ad-

vocate for dark matter haloes around galactic centres. The attempts being carried out to develop experiments capable of studying the characteristics of dark matter particles are often based on the identification of nuclear recoils produced by collisions between the theoretical WIMP particle and ordinary matter nuclei used as the detector target. Dark matter particles with masses from 10 to 10^4 GeV should present non-relativistic elastic scattering that would generate nuclear recoils in an energy range of 1 to 100's keV. The energy ranges that are of interest and from which the experimental design is engineered are the outcome of previous experimental results. The main developments have been obtained from experiments carried out from 2012-2015 whose objective was to set WIMP-mass-dependent upper limits on the WIMP-nucleon cross-section considering 10^{-43} to 10^{-45} cm^2 [1]. In this way, we are closer to establishing parameters in which to look for clues that would point us in the direction of a major breakthrough. The expected theoretical cross-sections in a nuclear recoil produced by WIMPs can reach values of about 10^{-12} pb. Detector technology has come a long way and now, thanks to the development of computational and statistical tools, we can work with different and creative detection methods. These methods are used to reduce and identify radiation similar to a WIMP's interaction that manifests itself as background. This background interferes with the signals and must be taken care of to retrieve reliable results in the data analysis. With the current technology, it is possible to work with cross-sections values across 8 orders of magnitude, from 10^{-4} pb to 10^{-12} pb. The experiment's design takes this information into account and saves its progress for future experiments that pursue direct dark matter detection [5].

In time, all the efforts currently taking place to detect dark matter and the evidence that supports it have helped state that the quark and lepton matter we are nowadays familiar with, constitutes only about 4.56±0.16 % of the present energy density of the Universe. Dark matter would constitute 22.7 ± 1.4 % of it leaving about $72.8^{+1.5\%}_{-1.6\%}$ to be considered as 'dark energy' [3]. In all, a dark matter and dark energy source is still unknown; the different manifestations of gravity include signs backing a new physical phenomenon but direct observations of it remain absent [3].

The bubble chamber technique would represent a direct detection of dark matter if successful. The bubble chamber takes place thanks to the behavior of super-heated liquids and its interaction with external particles. The PICO experiment benefits from the natural movement of the solar system basing it in the assumption that our galaxy is surrounded by a halo of dark matter from which plenty of particles travel through the bubble chamber detector. By doing so, we hope a small fraction of them will interact elastically with the fluid's nuclei and leave a small amount of energy which will result in the formation of bubbles. An analysis of these formations can take place thanks to the cameras in the detector and to the acoustic discrimination of the bubble formation on the active material, C_3F_8, caused by α-particles and nuclear recoils.

---

[1]XENON100, PICO, DARKSIDE-50, LUX

The materials used in particle detectors unavoidably contain traces of radionuclides, such as ^{238}U and ^{232}Th, which also add elements from their decay chains. The radioactive decays yield α, β and γ particles that produce direct or indirect background events. These yielded particles are not the only sources of background, cosmic rays and spontaneous fission of some radionuclides are also to be taken into account. In this range the nuclear recoils expected from WIMP scattering would have a similar energy spectrum to that of the background. This quandary could be avoided with a detector built from radio pure materials that would offer a clear WIMP signal detection.

Background event origins are numerous, the two main ones being neutrons and photoelectrons. Electronic recoils are produced by γ's and electrons, bubble chambers are insensitive to electron recoils. The recoils produced by cosmogenic and radiogenic neutron collisions with nuclei cannot be told apart from those originated by WIMPs. By carrying out the experiment deep underground, it is possible to stop most of the cosmogenic muons in the Earth's outer crust. As it has previously been mentioned, the discrimination and background control of nuclear recoils from radiogenic neutrons originating in the materials of the detector is a complex procedure.

This study focuses on PICO500. This will be a bubble chamber detector design to collect WIMP interactions data. It is expected to be the biggest of its kind. For the detector's design we need the energy spectrum of the radiogenic neutrons entering PICO500's volume and the simulation carried out with Montecarlo methods in the active volume. We want to make the nuclear recoils interactions negligible; this can be done by establishing the purity of the materials in the detector. There are different codes that have information about the flux of neutrons in different materials and compares it with neutron emission in (α,n) processes. The purpose of the study is to calculate the total number of radiogenic neutron generation from the detector's components and establish a minimum level of purity for which we can ensure 0.1 or less events per year from this source. The Montecarlo method is a strong tool incorporated in GEANT4 software. Estimations can be withdrawn from the number of events caused by nuclear recoils generated in the active liquid (C_3F_8) in a year. And so a standard for the material's purity can be determined to ensure a specific maximum number of events per year due to radiogenic activity . For this purpose in GEANT4 the models for PICO500 design have been developed, using this platform to define the basic geometrical structure. The composition for each material was described by previous experiments, NeuCBOT, a tool for (α,n) yield calculations, used this information to provide a neutron yield, that will later contribute to the activity calculations. With this, we could achieve an energy spectrum generated by (α,n) reactions and spontaneous fission. With these results, simulations can be carried out. The simulations will provide information about the activity within the detector. Then, a level of purity in the materials can be determined. This will dictate the number of events per year for different decay chains. The goal is to reach 0.1 events per year, a negligible number, so that the statistics concerning the detection method can still assure a trustworthy detection.

Chapter 1

Dark Matter

The work that has been invested in several observations and experiments has led us to the present hypotheses that seek to provide a sensible explanation to the phenomena. Dark matter is a favorable candidate because it is copacetic with current models that have been proven, and explores physics beyond the Standard Model. Its acceptance growth is expected after a series of evidences that call for an explanation that could be carried out with the concept of non luminous matter. This evidence comes from precise measurements of galaxy rotation curves, the calculations of galaxy clusters carried out via gravitational lenses, cosmic microwave background data and the abundance of light elements [1].

Dark matter can be complied with a variety of hypothesis, some of them are based in gravitational law modifications. Rotational velocities measured in galaxies can be described with Modified Newtonian Dynamic theories (MOND)[7] or their relativistic extension (TeVeS)[8]. But for larger cosmological observation scales, the theories do not hold. This was realized when structure formations and the CMB power spectrum were studied. MACHOs (Massive Astrophysical Compact Halo Objects) could be neutron stars, black holes, brown dwarfs or unassociated planets that emit little to no radiation[1] [9]. With 95% certainty we can rule out the idea of MACHO conforming the dark matter halo; microlensing observations in the Large Magellanic Cloud show that about 20% of the dark matter in our galaxy is composed of these kinds of objects [10]. The Big Bang Nucleosynthesis Model (BBN) predicts the abundance of light elements. It discards baryonic nature for dark matter since this range depends on the baryon density. This value is about $\Omega_b = 0.04$ which checks out with the value derived from CMB. It is estimated that the content of matter in the Universe is about $\Omega_M \approx 0.3$ [11] which possibly adds up considering baryonic dark matter is not affected by BBN and CMB constraints such as primordial black holes.

---

[1]They could be responsible for the large mass-to-light ratios detected in astronomical observations.
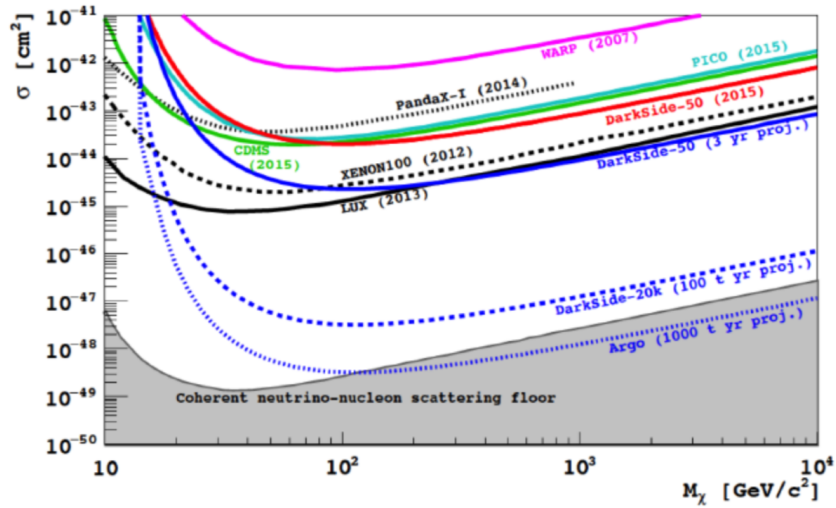
Figure 1.1: Results from direct dark matter search experiments in the WIMP-nucleon spin-independent cross section vs. WIMP mass plane [5]. Experimental limits are represented together with projected sensitivities (DarkSide-20k and Argo) that are expected to operate over the next years.

In figure 1.1 we can see the attempts to establish a region of experimental limits for WIMP-nucleon spin-independent cross section. These studies establish the sensitivity level we aim to work with to have reliable results. Scientists have braced themselves for dark matter's possible future validation. A sequence of cosmological simulations based in ΛCDM (Cold Dark Matter) have generated a structure of the Universe that tell us the percentages of its components. This model uses 6 free parameters to predict cosmic background radiation and describes a spatially flat Universe made of $4.56 \pm 0.16\%$ ordinary matter, $22.7 \pm 1.4\%$ dark matter and $72.8 \pm 1.5\%$ dark energy [3]. However this model is yet to be proven.

Even though dark matter has not yet been discovered, the parameters that characterize it have been laid out. Its nature is yet to be known, but there are clues regarding its behaviour and how to look for it. The quantum numbers and the interaction dark matter has with baryonic matter have produced a theory that would explain phenomena that cannot be described with our current understanding. The idea of physics beyond the Standard Model propels a very large range of studies. Since the mass ranges have not been specified, the variety of experiments being carried out is wide and each aims to find results in different magnitude orders.

The idea of a new particle to star the composition of this new kind of matter gained more and more appeal:

- In order to fulfill the dark matter parameters, the particles must be electrically neutral.

- The self-interaction in dynamical systems must be limited and include a collision-less component so that a weak self-interaction is featured. CMB and BBN predicts a non-baryonic nature since the Universe invests around 5% of its energy in ordinary matter.

- The mean life of the particle candidate must be long to leave a lasting footprint of dark matter in primordial CMB anisotropies and to have a considerable gravitational effect in galaxies.

1.1 Evidence

1.1.1 Bullet Cluster

The Chandra telescope presented one of the most convincing evidences of dark matter in 2006 [12]. This evidence consisted of the observation of the collision of two galaxy clusters shown in Figure 1.2. The demeanor of this event strongly shows the existence of two types of matter: ordinary matter and non-electromagnetic radiation emitting matter. During the collision, it was observed with gravitational lens techniques and x-rays that the gravitational potential did not behave as expected. The largest matter distribution was not where the visible matter was, instead it was past the site of the collision.

Figure 1.2: The Bullet Cluster: The result of a collision of galaxy clusters. The unique baryonic matter (pink) is shown; this distribution was obtained by means of x-rays. Dark matter (blue) is deduced from the calculations with gravitational lenses.

The most accepted explanation is that during the collision, the ordinary matter gas hit each other and stopped accordingly, leaving a trace of baryonic matter at the centre, however, dark matter went through this bulk and could be seen ending

up at opposite sides of the collision point. When this happened the gravitational potential did not follow the galactic gas as expected by the X-ray [13], instead, what was observed is that the potential followed the galaxies' distribution. This enforces the idea of general weak interactions except for gravitational force. However, it is not necessarily true.

1.1.2 Mass-luminosity relation in galaxies and clusters of galaxies

Frits Zwicky was a Swiss astronomer that measured the mass of galaxy clusters in 1933 using the Virial Theorem. This technique was used because galaxies and stellar over-densities in continuous fluids can be highly extended, it can be hard to define specific, finite measures of their mass and size. If we consider M the mass and L luminosity of a galaxy or cluster of galaxies, we can define $Y = \frac{M}{L}$ as a comparison parameter to that of the Sun denoted by $\frac{M_\odot}{L_\odot}$ [4]. For galaxies the range is around ten times $\frac{M_\odot}{L_\odot}$ and a hundred $\frac{M_\odot}{L_\odot}$ for clusters of galaxies. Zwicky was the first to notice that $Y = 100\frac{M_\odot}{L_\odot}$ and thus came with the idea of extra invisible matter to make up for the missing one. In modern times, this data is collected with gravitational lenses and X-ray measurements of the hot gas in the clusters. All this information sparked the idea of non-luminous matter since observations suggest masses' values larger than the Sun's where there is not enough visible matter to cause this phenomenon.

1.1.3 Galaxy Rotational Curves

Spiral galaxies have an spherical bulge at their centre and a thin disc that spreads to their furthest points. The tangential velocity v(r) of a star with mass m that tours in a galaxy of mass M(r) at a distance r from the galactic centre can be determined by matching the centrifugal and gravitational forces,

$$\frac{mv^2(r)}{r} = G\frac{mM(r)}{r^2} \tag{1.1}$$

$\longrightarrow$

$$v(r) = \sqrt{G\frac{M(r)}{r}}, \tag{1.2}$$

if ρ is the galaxy's density profile

$$M(r) = 4\pi \int \rho(r)r^2 dr. \tag{1.3}$$

For the spherical bulge at the centre M(r) $\propto r^3$ and for the extremities M(r)=constant, following this, at the centre of the galaxy, velocity v(r) should proportionally increase with r and decrease proportionally to $\frac{1}{\sqrt{r}}$ in the extremities [15]. However, Vera Rubin found this was not observed. In the 70's she measured v(r) for the Milky Way and other galaxies using Hydrogen's red shift. The observations showed that for r close to the extremities, M(r) $\propto$ r and so the rotational curves remain constant. An

explanation for this is that the galaxy's visible part is immersed in a dark matter halo that makes up for most of the total mass. The comparison can be appreciated in figure 1.3. This is one of the strongest ideas that back up dark matter theories [14].
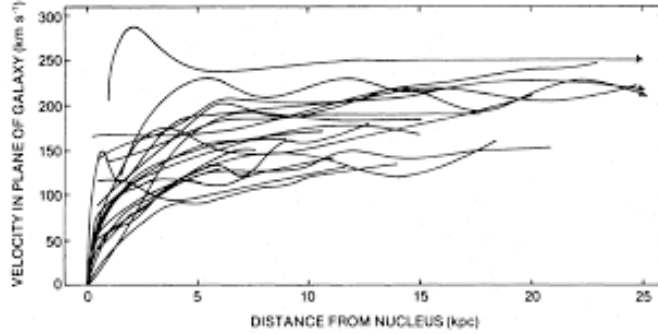
Figure 1.3: Curves of rotation of spiral galaxies such as the ones measured by Vera Rubin. Most galaxies show a flattening in speed when the radius is large.

1.1.4 Cosmic Microwave Background

In 1954 Penzias and Wilson discovered the Cosmic Microwave Background (CMB) while they were studying an unknown source noise in a radio antenna [16]. At the time they came to the conclusion that the radiation was the remainder of what survived when photons decoupled from matter in the early Universe. The CMB spectrum can be modeled with black body radiation taking T=2.7255 K. There have been several experiments carried out with satellites like COBE, WMAP and Planck that found that the CMB has an isotropic nature of up to one part in a million. The small deviations of temperature in a n-direction can be expanded in spherical harmonics [15].

$$\frac{\Delta T(\mathbf{n})}{T} = \sum_{l=0}^{\infty} \sum_{m=-l}^{+l} a_{lm} Y_{lm}(n) \tag{1.4}$$

The relation is described with the directions m and n separated by θ such that $n \cdot m = cos\theta$. You can get the correlation function $C(\theta)$ by averaging all the directions separated by θ. This function can be expanded in Legendre polynomials [15],

$$C(\theta) = \left\langle \left(\frac{\Delta T(n)}{T}\right)\left(\frac{\Delta(n)}{T}\right)\right\rangle = \frac{1}{4\pi}\sum(2l+1)C_l P_l(cos\theta) \tag{1.5}$$
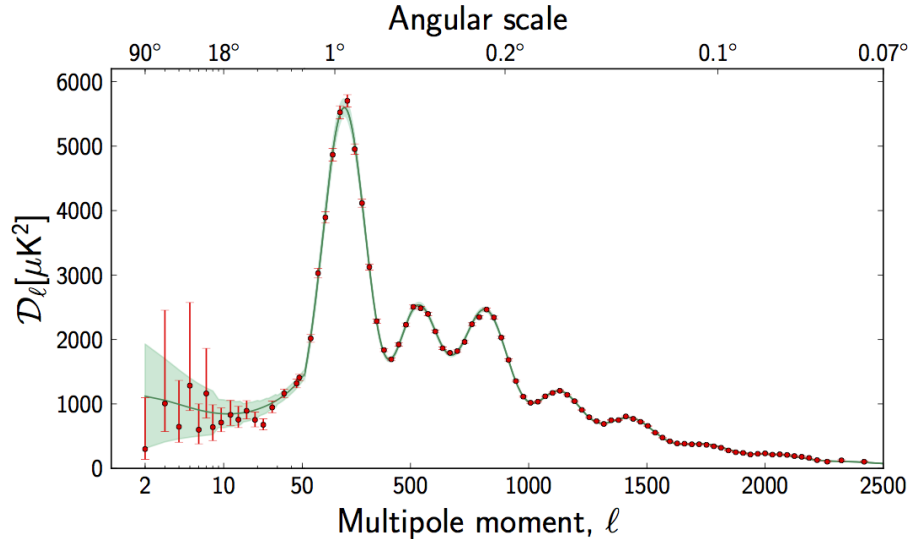
Figure 1.4: Power spectrum of the fluctuations of temperature of the CMB observed by the Planck Satellite. Fluctuations are plotted at different angular scales. The red dots with error bars are the satellite's data, the green region represents the Standard Model of Cosmology (ΛCDM).

From equation 1.5 we can obtain information of cosmological parameters that in return gives us data of the Universe's composition. This way we know that about 4.56% of it is made of ordinary matter, deduced from the first peak in figure 1.4 and from the fits of the second and third peak about 22.7% of of matter is non-baryonic matter.

1.1.5 Gravitational Lenses

The path of a photon can be affected by an object's mass M at a minimum distance b. The deviation can be denoted by the angle $\alpha = 4\frac{GM}{bc^2}$. In this case, the object is acting as a gravitational lens when compared to optic lenses, here the mass can be determined by the deflection angle [17]. If the object is large enough, it is possible to observe multiple images of the photon source. This technique is known as strong gravitational lensing and works with galaxies and clusters of galaxies. When photons pass several objects acting as gravitational lenses in their way to Earth to be observed, they provide detailed information about distribution of matter regardless of its nature; this is weak gravitational lensing and it is especially good for acquiring dark matter data. There are also gravitational micro lenses. Applying this technique for stars in the Milky Way the deflection of light is too small to be accurately measured, but it is possible to collect data of transitory small changes in the source's luminosity [15].

1.1.6 Primordial Nucleosynthesis

The early Universe model is strongly supported by the Big Bang's Nucleosynthesis. In this model we consider large amounts of light elements such as D, ^{3}He, ^{4}He and ^{7}Li

synthesized after the first three minutes after the Universe was created [18]. This is supported with observational data about the Universe's composition. At the beginning, the weak interaction made it possible for protons and neutrons to be in thermal equilibrium.

(t = 10^{-2} s):
$$n + \nu \longleftrightarrow p + e^- \qquad\qquad n + e^+ \longleftrightarrow p + \bar{\nu}_e \qquad\qquad (1.6)$$
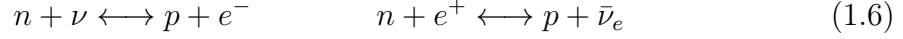
When the energies are about 0.1-0.3 MeV almost all the neutrons turn into ^{4}H by the next reactions, (t = 1-3 min):

$$n + p \longleftrightarrow D + \gamma \qquad D + D \longleftrightarrow He + \gamma \qquad D + p \longleftrightarrow^3 He + \gamma \qquad D + n \longleftrightarrow He + \gamma \tag{1.7}$$

So the mass fraction of ^4He is given by,

$$Y = \frac{4N_{He}}{4N_{He} + N_H} \approx 0.24 \tag{1.8}$$

The most recent data suggests that $Y = 0.2551 \pm 0.0022$. Using spectroscopy in regions close to red shift for He_I high density regions the abundance of ^7Li and D have been determined. Considering this data and the calculations for baryogenesis, $\Omega_b h^2$ has restricted values:

$$0.018 < \Omega_b h^2 < 0.023 \tag{1.9}$$

This result agrees with Planck's experiments outcome but differs from the expected total baryonic density $\Omega_b h^2 = 0.308 \pm 0.012$. This discrepancy is an evidence for dark matter [3].

1.2   DM Properties

We have come a long way regarding the quantity and distribution of dark matter. Aforementioned, even though dark matter has not been directly observed, several dark matter studies provide a lot of information in which we can obtain data regarding the particle's nature. To reproduce the Primordial Universe's levels of light elements, we need to consider non-baryonic matter that would not interact electromagnetically. There are several cosmic observations in this regard that support this idea, such as the baryonic acoustic oscillations seen in the formation of cosmic structures. Aside from cosmic observations, there are also simulations of the cosmic structures of the Universe that agree with the mentioned observations when we consider non-relativistic matter or sufficiently massive structures. Observations from the Bullet Cluster tell us that the dynamics cannot be explained with gravitational modifications. Also, after the early Universe cooled down, the observed density Ω_{MO} of the Cosmic Microwave Background requires stable matter [19].

The strategies to abide this problem introduces a new branch of thought within

particle physics and asks for a solution beyond the Standard Model. To explain these evidences we need stable, neutral, non-baryonic, with no electromagnetic interactions and massive particles. There are no particles with all these characteristics in the Standard Model but it had helped by engulfing a series of attributes to look for and that generates several theoretical proposals to work with. The Standard Model theory had unsolved questions long before dark matter came by: the hierarchy problem, number of parameters within the Standard Model, grand unified theories, the muon's anomalous magnetic moment and the strong CP problem. These problems were somewhat patched with parameters out of natural scales or ignored, remaining as big physics mysteries; but now, dark matter could represent a possible elegant way to solve them [19]. The dark matter candidate particles are within the mass range of $10^{-31} < m_\chi < 10^{48}$ GeV [63].

1.3 Candidates

The problem within particle physics regarding the previous enigmas is yet to be solved. None of the Standard Model disputes have been explained and the observations gathered suggest that we are missing something. Dark matter would be an innovative explanation for these predicaments. This situation has prompted high energy physicists and cosmologists to come up with attractive ideas and theories that would clear everything up [19].

1.3.1 Baryonic Matter

A first approach to what we now call dark matter contemplated objects made up of assorted non-luminous astrophysical bodies, such as planets and neutron stars. In this context, the micro-gravitational lensing was an extremely useful technique to try to find dark matter in the form of big objects called MACHOs (MAssive Compact Halo Objects). These experiments have established a mass limit from 0.15 to 0.9 solar masses by considering them as brown dwarfs, neutron stars, white dwarfs or black holes [20]. Primordial black holes in the range 10^{23}–10^{31} kg as a strong candidate for dark matter have been discarded thanks to the use of gravitational lenses [21].

1.3.2 Sterile Neutrino

In 1994 Dodelson explained the discrepancies of the ΛCDM Model (Lambda Cold Dark Matter) and the observations of cosmic structures 1-5 Mpc away by proposing sterile neutrinos as hot dark matter candidates [22]. This particle candidate only interacts gravitationally, completely giving up any other kind of interaction considered in the Standard Model. Within this theory the developed models and global experimental data exclude the permitted parameter regions for $\Delta m^2 = 1$ eV^2 and $sin^2(2\theta_{24}) = 0.1$. Here the anomalies in ν_μ and $\bar{\nu}_\mu$ oscillations are observables of the model. The IceCube experiment didn't find any anomalies while looking for sterile

neutrinos [23], but it settled a range for $\Delta m^2 = 0.3$ eV^2 and $sin^2(2\theta_{24}) \leq 0.02$ in a 90% C.L. allowing for new experiments with a more precise range [24].

1.3.3 WIMP

WIMP is a very strong candidate for dark matter particle. Its name comes from the acronym that describes the expected nature of this particle: Weakly Interacting Massive Particle. As such WIMP should have a series of properties. As has been mentioned, they should have a weak interaction with ordinary matter. Additionally, thermal and chemical equilibrium with quarks and leptons in the early Universe is expected, to form the relic density we observe presently. This could be formed when decoupling by changing their velocities to non-relativistic margins [25]. If ν is the WIMP's annihilation relative velocity and $\langle \sigma_{ann\nu} \rangle = 3 \times 10^{-26} cm^2 s^{-1}$ an average of the thermal WIMP's distribution, the relic density is considered to be

$$\Omega h^2 = 3 \times 10^{27} cm^3 s^{-1} \frac{1}{\langle \sigma_{ann\nu} \rangle}. \tag{1.10}$$

Here the given average is in the weak interactions' order. The result is independent of the WIMP's mass and comes from cosmological calculations. This cosmological consequence of fixing it in the electroweak scale gives this candidate a privileged status in the dark matter theories [26]. Some particular WIMP examples are:

- the lightest neutralino

- Kaluza-Klein particles in extra dimensions theories

- particles that arise in theories that seek to stabilize the Higgs Boson mass

1.3.4 Supersymmetry

Supersymmetry is a theory beyond the Standard Model. Here an extension of the established model is done and we associate for each particle a *super-particle* with a $|S - 1|$ spin. For each boson there is a *super-particle* fermion and for each fermion a *super-particle* boson, so then the fundamental interaction mediators that make up the matter's components become indistinguishable. With these kinds of particles, the supersymmetric extension needs to adapt and acquire minimal conditions to operate, one of which introduces a new quantum number (R) that distinguishes *super-particle* from particles:

$$R = (-1)^{3B+L+2S} \tag{1.11}$$

Here B is the baryonic number, L the leptonic number and S the spin. Superymmetric particles decay in an odd number of *super-particles* plus Standard Model particles. The Z boson, photon and neutral Higgs *super-particles* have the same quantum numbers and can mix into a neutral, stable and a half integer spin particle called the lightest neutralino (LSP):

$$\chi = N_{11}\tilde{\gamma} + N_{12}\tilde{Z} + N_{13}\tilde{H}_0^1 + N_{14}\tilde{H}_0^2 \tag{1.12}$$

Where $\{N_{nm}\}$ are the parameters in the mixing matrix in the supersymmetric model. χ mass range goes from GeV to 10 TeV and this made it a favourite as a WIMP particle, nonetheless, direct detection of dark matter has been unsuccessful and caused a reformulation of supersymmetric particles with more natural masses. By applying phenomenological restrictions the parameters are reduced from 100 to 19, additionally we get new particle candidates like the higgsino and the wino that locate the mass range between 35 and 155 GeV/c^2. These values are within current experimental detection ranges [27].

1.3.5 WISP

These candidates are part of the cold dark matter theories that state a very weak interaction with ordinary matter and whose energies are in sub-eV. Strong candidates are axions coming from quantum chromodynamics, Axion Like Particles (ALP) with masses between 0.1 - 100 meV and dark photons with $\leq$ 100 meV energies [28].

1.3.6 Axions and ALP

Charge-parity (CP) symmetry is expected to be violated in QCD vacuum from the strong interaction of quarks and gluons. This violation was studied by Hooft, and implies a big electric dipole moment for the neutron. Experimental verification is yet to be found as attempts to verify it had failed and it has never been observed, thus, CP symmetry is not violated by QCD [29].

Later in 1977, Peccei and Quinn came up with a mechanism to solve the strong CP problem in QCD [30, 31]. Here, a new chiral symmetry is introduced U(1) to make up for the CP violation by instantly breaking into an energy scale f_a. This implies the existence of a pseudoscalar particle known as axion. Axions could have been generated in the early Universe, where they acquired mass during the QCD phase transition that went on when the quark-gluon plasma condensed into hadrons [32]. If, the axion's mass is between 10^{-3}-10^{-6} eV [25] they make good congruent candidates. Astrophysical observations place the axion's mass under 15 meV, the lower limits come from cosmology and their value depends on the thermal history of the Universe. Axions in the electroweak scale are experimentally discarded [33].

Other theories regarding axion-like particles have also been developed in string theories interacting with the Standard Model through electromagnetic decoupling. This decoupling depends on the mass for QCD axions and is independent for ALP. The current axion and ALP experiments are based in the axion-photon conversion under the influence of external electric and magnetic fields.

1.3.7 Dark Photon

Grand unifying theories and string theories predict the existence of dark photons. These are particles with an energy range between MeV and GeV associated to a new

fundamental interaction similar to electromagnetism known as *dark force*. Dark Force has a symmetry group U(1). The existence of dark photons can potentially explain the discrepancies between the experimental and theoretical results of the muon anomalous magnetic moment [34].

Chapter 2

Detection of WIMP

2.1 Direct Detection

Direct detection experiments are based on the movement of the solar system around the Milky Way through an assumed halo of dark matter [35]. The halo's properties are important for the experiments design. The observations of "satellite galaxies" around their host galaxies gives data, based in their rotation velocities, of dark matter clusters extending beyond the galactic core. Considering the Standard Halo Model, halos are spherical, isothermal, isotropic and in a steady state linked to the Maxwell-Boltzmann distribution [35]. The density distribution needs to be proportional to r^2 to fit the rotation curves. This is why the detection experiments attempt to take advantage of this by aiming to detect the halo's particles in which Earth is immersed. A large number of WIMP particles is expected to go through the experiments' target material. If a WIMP's number density is denoted by n, the dark matter halo velocity is typically the order of the galactic rotation $v = 300\frac{km}{s} \sim 10^3 c$, and the local dark matter density is $\rho_0 \simeq 0.3\frac{GeV}{cm^3}$ [36] then the WIMP flux (ϕ) is,

$$\phi = vn = \frac{v\rho_0}{m_\chi} \simeq \frac{10^7}{m_\chi(GeV)}\frac{1}{cm^2 s} \tag{2.1}$$

The number of WIMP traveling through the detector is tremendous and we hope that a small portion of them will disperse elastically with the nuclei in the active material of the detector. Several experimental attempts have been designed to try to detect and quantify the small amount of energy left from the nuclei's interactions. The developed techniques are varied and each of them consider different aspects and are trying to find different WIMP candidates. By taking the WIMP mass to be 100 GeV, 10^5 dark matter particles are expected to cross a square centimeter per second, 10^{23} WIMPs reaching the Earth each second. The direct detection techniques are based on the possible signals produced by elastic scattering of dark matter particles coming from the halo and the nuclei in the active material of the detector. The deposited energy by the recoiling nucleus can be described by [37]

$$E_R = \frac{1}{2}m_\chi v^2 \frac{4m_\chi m_N}{(m_\chi + m_N)^2}\frac{1 + cos\theta}{2}. \tag{2.2}$$
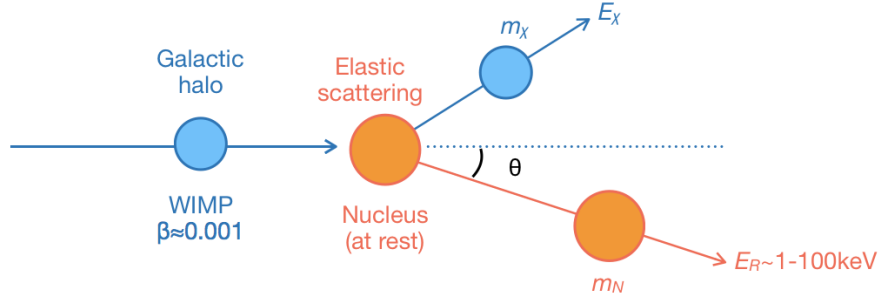
Figure 2.1: WIMP-nucleus scattering [38]. The energy E_R is the recoil energy, m_χ and m_N the WIMP and nucleus masses respectively and θ the scattering angle. The expected recoil energy range is between 1 to 100's of keV.

The recoil energy, depends on the incident WIMP energy, on the WIMP and nucleus masses and on the scattering angle. This leads to a few keV and a few hundred keV energy range for WIMP within the 100 GeV mass order. The peak energy happens during a head-on collision, when the mass is equal to the target mass. Both masses are the same value implying,

$$E_{R_{max}} = \frac{1}{2}m_\chi v^2 = \frac{1}{2}\left(\frac{m_\chi}{1GeV}\right)keV \approx 100keV. \tag{2.3}$$

However, this recoil energy value can also be produced by lighter particles with higher velocities such as neutrons. This similarity makes it really important to come up with crafty, effective approaches to deal with the overwhelming background.

2.1.1   WIMP nuclear recoils

WIMP differential event rates for nuclear recoils can be set by [39, 40]

$$\frac{dR}{dE_R} = \frac{\rho_0}{m_\chi m_N}\int_{\nu_{min}}^{\infty} \nu f(\nu)\frac{d\omega}{dE_R}(\nu, E_R)d\nu. \tag{2.4}$$

Where ρ_0 is the WIMP local density. Here the differential section $d\omega$ and the energy effective section for a WIMP-nucleus scattering are given in terms of $f(\nu)$, the velocity distribution for the WIMP, normalized to the unit. The important information concerning the WIMP interactions with atomic nucleus is contained by the effective section described with the energy change rate $\frac{d\omega}{dE_R}(\nu, E_R)$.
Taking into account the elastic dispersion of a WIMP-nucleus collision in the centre of mass reference frame,

$$E_R = \frac{\mu_N^2 \nu^2(1 - cos\theta)}{m_N} \tag{2.5}$$

in which we are considering the reduced mass of both objects, $\mu_N = \frac{m_\chi m_N}{m_\chi + m_N}$. There is also a minimum velocity at which a nuclear recoil occurs used in the integral limits,

$$\nu_{min} = \sqrt{\frac{m_N E_{threshold}}{2\mu_N}}. \tag{2.6}$$

The threshold energy is defined by the detector. The integral's upper limit is infinity, however the actual maximum velocity is the escape velocity v_{esc} at which WIMP are gravitationally linked to the Milky Way in its frame of reference. The total number of events (per kg per day) is calculated by integrating the differential event rate considering all possible energy spectra of the nuclear recoils [39]

$$R = \int \frac{dR}{dE_R} = \int_{E_{threshold}}^{\infty} \frac{\rho_0}{m_N m_\chi} \int_{\nu_{min}}^{\nu_{esc}} \nu f(\nu) \frac{d\omega}{dE_R}(\nu, E_R) d\nu. \tag{2.7}$$

We can separate (2.7) into different components and analyze them accordingly based on various studies,

- **Particle and Nuclear Physics**: $\int_{E_{threshold}}^{\infty} \frac{\rho_0}{m_N m_\chi}$

  Information regarding WIMP-nuclei interactions is contained in the cross-section $\frac{d\omega}{dE_R}(v, E_R)$. An effective Lagrangian can use scalar, vector or axial coupling to describe the WIMP-quark interaction. For the scalar and vector cases, the effective section for WIMP-proton interactions plays an important role in the spin independent part and is proportional to the number of nucleons squared. The axial case produces the spin-dependent part which can be denoted by a function including the WIMP's spin and the nucleus' angular momentum. When nuclear wave functions are added to the WIMP-nucleus cross section, its coherence is also considered,

$$\frac{d\omega}{dE_R} = \left(\frac{d\omega}{dE_R}\right)_{SI} + \left(\frac{d\omega}{dE_R}\right)_{SD} \Rightarrow \frac{d\omega}{dE_R} = \left(\frac{m_N}{2\mu_N^2 \nu^2}\right) \left[(\sigma_0^{SI} F_{SI}^2(E_R)) + (\sigma_0^{SD} F_{SD}^2(E_R))\right]. \tag{2.8}$$

σ_0^{SI} and σ_0^{SD} represent the cross sections for spin-independent and spin-dependent, respectively, when there are zero transfer moments. The F functions are the form factors that code the dependency in the momentum transfer that depend on the nuclear recoil energy. Generally,

$$\sigma_0^{SI} = \frac{4\mu_N^2}{\pi}[Zf^p + (A - Z)f^n]^2 \tag{2.9}$$

$$\sigma_0^{SI} = \frac{32\mu_N^2}{\pi}G_F^2 \frac{J+1}{J}[a^p\langle S_p\rangle + a^n\langle S_n\rangle]^2. \tag{2.10}$$

where Z is the atomic number, A the atomic mass and J the angular momentum. The effective Langrangian can be used to calculate the WIMP coupling with neutrons and protons in the spin independent and dependent cases: f^p, f^n and a^p, a^n. $\langle S_p\rangle$ and $\langle S_n\rangle$ are the expected values for the spin operators of the proton and neutron in the zero momentum transfer, they are determined by using nuclear models [41].

- **Astrophysics**: $\int_{\nu_{min}}^{\nu_{esc}} \nu f(\nu)$

  The halo density is important to take into account. In the Standard Model of the dark matter halo, the WIMP local density can be $\rho_0 \equiv \rho/(r = R_0)$. Here R_0 is the distance between the Sun and the Milky Way's centre, about 8.0 ± 0.5 kpc. The velocity distribution considered is that of Boltzman in terms of an isothermic particle sphere:

  $$f(\nu) = \frac{1}{\sqrt{2\pi\sigma_\nu}} exp\left(-\frac{\nu^2}{2\sigma_\nu^2}\right). \tag{2.11}$$

  Here, the local circular velocity is related to the dispersion velocity via

  $$\sigma_\nu^2 = \sqrt{\frac{2}{3}}\nu_c \qquad \text{with} \quad \nu_c \equiv \nu(r = R_0). \tag{2.12}$$

The WIMP-nucleus elastic collisions idea could provide irrefutable signals that would give information about the dark matter halo in astrophysical studies. However, this data would depend enormously on the active material mass and the WIMP mass; this mass dependency shows an energetic dependence. Energy dependence is due to kinematics and WIMP velocity distribution. The WIMP recoil rate is a function of the WIMP mass, the target mass and the form factor. The Earth's movement in the galactic frame of reference would also display an event rate R with temporal, spatial and directional dependence.

Considering the halo theory within the Standard Model hypothesis of the halo of dark matter [40, 41], we see that the differential rate of events is decribed by,

$$\frac{dR}{dE_R} = \left(\frac{dR}{dE_R}\right)_0 F^2(E_R) exp\left\{-\frac{E_R}{E_c}\right\}. \tag{2.13}$$

In the limit of energy $E \longrightarrow 0$ keV, E_c is the characteristic energy that depends on a characteristic parameter of the active material.

Temporal dependence evidence is one of the strongest arguments backing dark matter theories. The dark matter halo model is considered to be static around the Milky Way. During summer, the velocity of Earth and Sun add, in winter they subtract. This gives cosinusoidal signals for dark matter in the differential event rate over the course of a year, known as annual modulation [26, 40],

$$\frac{dR}{dE_R} \approx \left(\frac{d\bar{R}}{dE_R}\right)\{1 + \Delta(E_R)cos[\alpha(t)]\} \tag{2.14}$$

taking $\alpha(t) = \frac{2\pi(t-t_0)}{T=1year}$ and $t_0 \sim 150$ days.

The distribution of dark matter is affected by gravity, including the Sun's gravity

within our Solar System. This gravitational focusing includes a gravitational potential coming from the Sun that deflects dark matter and that increases its density and velocity as the Sun moves. Thus the distribution of dark matter changes, increasing in March when Earth is behind the Sun and decreasing when this position switches in September. In conjunction with the annual modulation, the gravitational effect fluctuates the differential event rate through the year.

Galactic reference frames do not have a preferential direction for movement, but it has to be taken in mind the laboratory's frame of reference. The flux of dark matter points at the Sun's movement direction; hence the differential event rate should point to the opposite side. The WIMP rate can be described by the nuclear recoil energy and the angle (γ) between the velocity and the WIMP so the direction is,

$$\frac{dR}{dE_R \, dcos\gamma} = \frac{\rho_0 \sigma_{WN}}{\sqrt{\pi}\sigma_\nu} \frac{m_N}{2m_\chi\mu^2} exp\left\{ -\frac{[(\nu_{orb}^E + \nu_c)cos\gamma - \nu_{min}]^2}{\sigma_\nu^2} \right\}, \qquad (2.15)$$

where ν_{orb}^E is the horizontal component for Earth's velocity parallel to the Solar movement direction [26, 40].

2.2   Indirect Detection

Indirect detection is based on the detection of Standard Model particle signals of the radiation caused by the WIMP's decay or annihilation [39]. The main possible particles interacting in these experiments are:

- *Gamma Radiation*
  The data on this kind of radiation can be gathered by Cherenkov telescopes on Earth and gamma radiation detectors coupled to space stations. Most experiments for dark matter detection involve the Milky Way's centre and dwarf spheroidal galaxies because these are the regions that are most likely to produce detectable signals.

- *Ultra-High Energy Neutrinos*
  When a WIMP annihilation occurs in the Sun or decays in its path to Earth, it can be detected by studying the muons decay chain. For this, the Sun and the Milky Way's centre are the main objects of study.

- *Antimatter*
  This includes particles emitted from the dark matter halo such as positrons, antiprotons or antideuterons.

Indirect detection of dark matter has led to several anomaly reports. The interpretations derived from this have brewed new ideas for dark matter particle candidates that have caused polemic arguments that have been gradually cleared out.

2.3 LHC

The LHC's endeavor towards dark matter detection is persistent in their pursuit to reproduce the "freeze out" phenomenon of WIMPs. By colliding Standard Model particles, the LHC seeks to invert the annihilation process. According to supersymmetric theories, dark matter particles are produced in the ensemble of standard model particles interactions, therefore there is no direct relation for the annihilation and production processes. The strategy consists of trying to produce a WIMP particle (χ) with $pp \longrightarrow \chi\bar{\chi}$ [39]. The WIMP particles would be detected by an imbalance in the total transverse momentum E_T and a mono-object presence (X). The objects denoted by X could represent particles such as Higgs, photons, W, Z^0, etc. To identify the mono-X interactions, special techniques are required to obtain enough information during the $pp \longrightarrow \chi\bar{\chi} + X$ reactions [42]. Kinematic approaches are usually the most popular because they can be graded with theoretical models and experimental data. Results showing an excess in the kinematic distributions could be attributed to dark matter particles. Other ways to try to find dark matter includes top quark pairs and Higgs boson decay [39].

The efforts being carried out are unlikely to provide direct evidence of dark matter particles, however, this, combined with other projects can be conclusive. The experiments can provide crucial information such as its quantum numbers, effective cross-section, mass, etc. This data can be used in direct detection projects and lead to important delimitations in the experiment's design.

Chapter 3

Super-heated Liquid Detectors

Visualization of nuclear and elementary particle phenomena has a vital role in tech development for new detection techniques that lead to data reception and enables further study of these fields. The first trials were carried out with cloud chambers and photo emulsions. In the years that followed, the super-heated liquids technology developed bubble chamber experiments as a procedure to design experiments that expand our understanding of the Standard Model.

3.1   Bubble Chambers

Daniel Glaser invented the bubble chamber in 1951. This development signified the direct observation of results from particle interactions on a macroscopic scale. Since then, the necessity to come up with experiments that would give signals from particle physics phenomena on a bigger scale was covered. Later on, this technique incorporated cosmic ray detection [43].

Bubble chambers are devices that have an super-heated liquid on the verge of boiling but due to pressure control, it does not. It is highly sensitive and when the right amount of energy is introduced, however small it may be, it reacts by producing a bubble leaving its metastable state. This occurs when particles that go through the active material interact with its nuclei and deposit energy.

This technology endorsed several discoveries because of its capability to let us visualize what was going on in the material by describing fundamental particles and their interactions. This was further developed by introducing cameras to the bubble chambers that would document the particle beams by synchronizing them with the chamber so it would fire at the right time. When magnetic fields were immersed in the detectors, it helped identify the particles involved with the Larmor ratio. Glaser's first attempts to explain the function of the bubble chambers with electrostatics failed. Frederick Seitz came up with a thermodynamic scheme that explained the operation in the Hot Spike model [44].
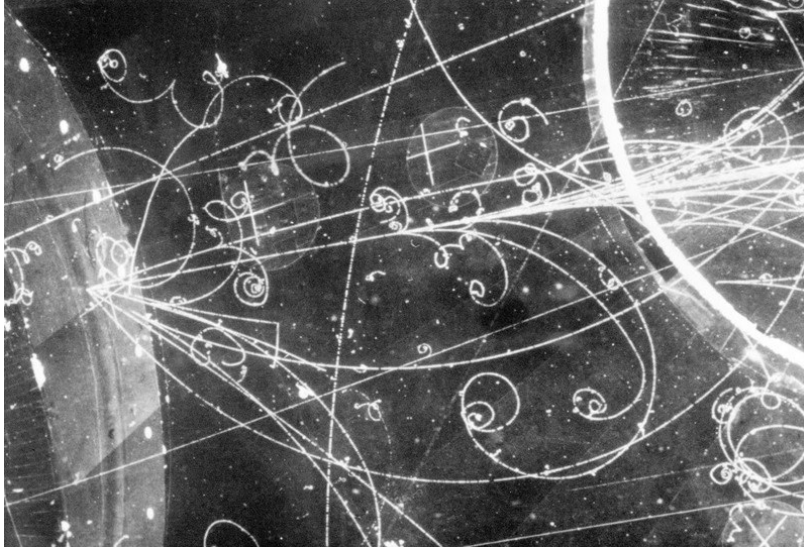
Figure 3.1: Bubble Chamber Trajectory example of different particles such as electron-positron pairs.

3.1.1   Hot Spike Model

Hot Spike refers to the heat transfer due to energy transfer produced by any means in the super-heated liquid [44]. This produces a pressure increase in the vapour at a local level. The vapour pressure has to be higher than the superficial tension of the liquid. This leads to a break of equilibrium that maintains both phases separated and enables the production of a bubble. The energy exchange that takes place in the active liquid interactions can deposit enough energy to form a bubble causing the transition from liquid to gas state. This produces a round cavity with a certain radius R that would minimize the superficial tension. Given sufficient energy the liquid will turn into vapour and the bubble will expand; if not, the bubble will collapse and there will not be a phase transition.

3.1.2   Critical Radius

The critical radius (r_c) of a bubble is defined by the Gibbs condition; it is the radius value in which the difference of pressure throughout the surface is balanced by the superficial tension σ [45]. Taking P_b as the pressure within the bubble and P_l the pressure of the liquid we have that,

$$P_b - P_l = \frac{2\sigma}{r_c}. \tag{3.1}$$

P_b is normally the vapour's pressure. If the radius is smaller than r_c it will progressively increase until the inside reaches just below the boiling point temperature in the given pressure conditions.

3.1.3 Critical Energy

The energy spectrum present also plays an important role in the formation of bubbles. The energy E_r, of the particle has to be greater than a fixed critical energy E_c. It also needs to have sufficient stopping power in order to produce the required amount of heat within the critical radius. In terms of energy, enough is needed to cover both the heat to vapourize the fluid and to form the bubble's surface, which are described in the following equation,

$$E_c = 4\pi r_c^2 \Big(\sigma + T\frac{d\sigma}{dT}\Big) + \frac{4\pi}{3}r_c^3\rho_b\Delta h, \tag{3.2}$$

where ρ_b it's the bubble's inner density, $\Delta = h_b - h_l$ is the fluid's specific enthalpy and T the temperature. With this, by controlling the temperature and pressure, the critical energy can be fixed so that the energy deposited by the interactin particles will guarantee a bubble formation by a period of phase transition from liquid to gas described by

$$E_{dep} = \frac{dE}{dx}L_c \geq E_c. \tag{3.3}$$

The L_c refers to a critical length that depends on a dimensionless parameter whose nature we are yet to fully understand [46].

3.1.4 Bubble Chambers as Dark Matter Detectors

Due to technology limitations, dark matter detection experiments were not very efficient since the enormous amount of electromagnetic background made it almost impossible to obtain reliable signals. The techniques that discriminated the background were not good enough. In the 90's, bubble chambers were proposed as a solution to this problem since it eliminates the unwanted electromagnetic background [47].

The design of the bubble chambers had to be modified and adapted to serve this purpose. The small probability of an interaction between dark matter and baryonic matter changes the nature of the devices, from being a multiple paths register, to being a counting mechanism. In the last two decades the super-heated liquid models have been developed as dark matter detectors.
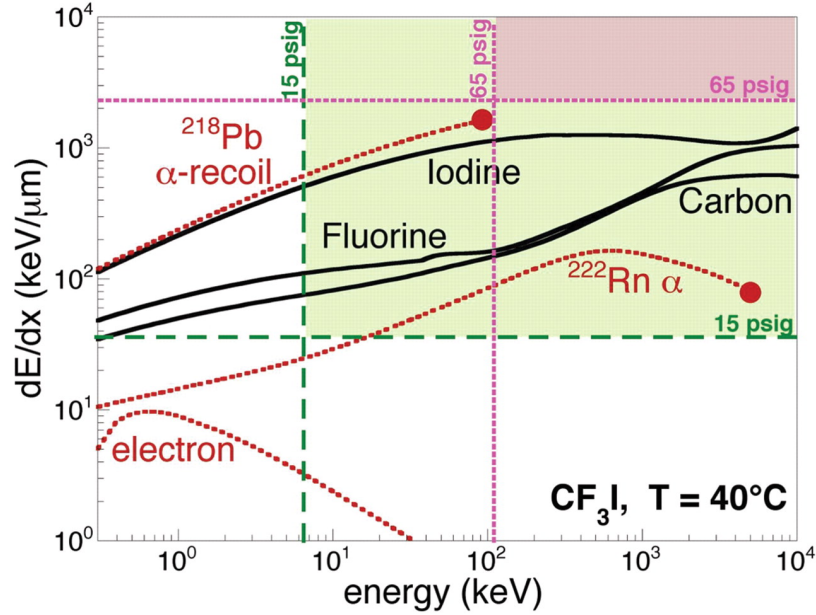
Figure 3.2: Instant stopping power vs. energy for different particles.

Figure 3.2 shows in green and pink regions the corresponding values of $\frac{dE}{dx}$ and the threshold energies for which the nucleation of bubbles takes place in temperatures of 40°C. According to Seitz Theory [44], the nucleation of bubbles will occur only when the super-heated fluid is at the pressures within the coloured regions. It also highlights the impossibility of nucleation due to electrons.

3.2   PICO Experiments

PICO experiments are collaborative efforts to find evidence of the WIMP particle. PICO was formed in 2012, by the merger of two parent organizations: PICASSO: Project In Canada to Search for Supersymmetric Objects and COUPP: Chicagoland Observatory for Underground Particle Physics. This collaboration includes several universities and organizations in collaboration with PICO and SNOLAB, some of which are Northwestern, University of Toronto, Université de Montréal, Pacific Northwest National Laboratories and several others from various states in the U.S. and Canada, including other countries abroad such as Mexico.

The PICO experiments are bubble chambers devised and designed as dark matter detectors. The experiments have been conducted in SNOLAB, a facility two kilometers underground. Some of the SNOLAB projects involving bubble chambers are COUPP4, PICO-2L, PICO-40 and PICO-60 experiments. These,either have been carried out or are currently active; PICO-500 is being designed. The difference between them is mainly the size of the active liquid's container aside from some design modifications.

3.2.1 Detector Description

The experimental layout in the models is similar. There is a steel tank containing water that defines the largest dimensions of the experimental parts. Inside, there is a stainless steel pressure vessel containing mineral oil in which a quartz jar is submerged. This jar contains the active liquid, C_3F_8, in which the WIMP-nuclei interactions would take place.

There are cameras using CMOS technology to take pictures from solid angles of $60°$ at a rate of 600 fps. These images are used to identify the bubbles and reconstruct the spatial coordinates in the quartz jar. To provide sufficient light for the pictures, there are some LEDs used as flash light that would increase luminosity by reflecting in the retro-reflector sheet around the container's surface. To listen to the acoustic emissions produced by the bubbles during the WIMP-nuclei interactions, some piezo acoustic transducers are attached to the container supported by a PVC ring.

There is an external hydraulic system that controls the pressure in the experiment. A system of stainless steel bellows balance the pressure between the hydraulic fluid and the active substance. The pressure vessel inside the water tank isolates the C_3F_8 from radiation and at the same time works as a temperature regulator.

- **PICO-60**
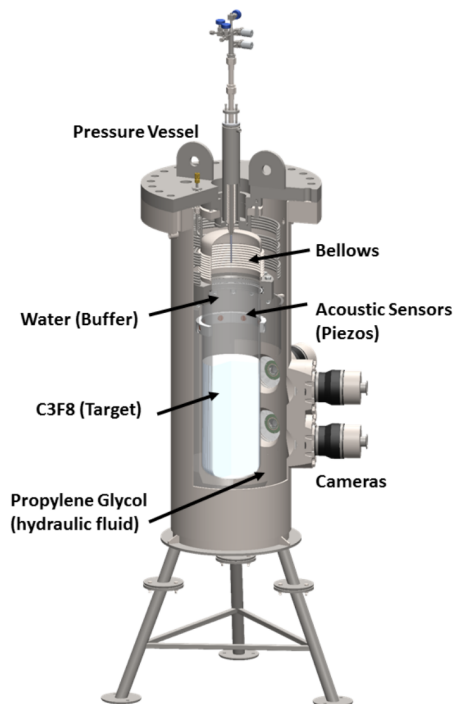
Figure 3.3: Visualization of the inside of PICO-60 bubble chamber.

PICO-60 experiment was the biggest bubble chamber used as a spin-dependent dark matter detector in the world. It is made up of a quasi-cylindrical synthetic

silica container with a diameter of 30 cm and a length of 1 m. It contained 52.2 $\pm$ 0.5 kg of C_3F_8; C_3F_8 has not been the exclusive active material. For PICO-60 first run, CF_8I was used instead. The active material selection is an important part of the detection process since the signals come from this part of experiment.

The bubble chamber is submerged in ultra-pure water to insulate it from the stainless steel surface of the pressure vessel that surrounds it. Its container is sealed on the top by flexible bellows. The pressure vessel has a diameter of 60 cm and a height of 167 cm. There are 4 windows that enable cameras have visuals of the synthetic silica container.

- **PICO-40**
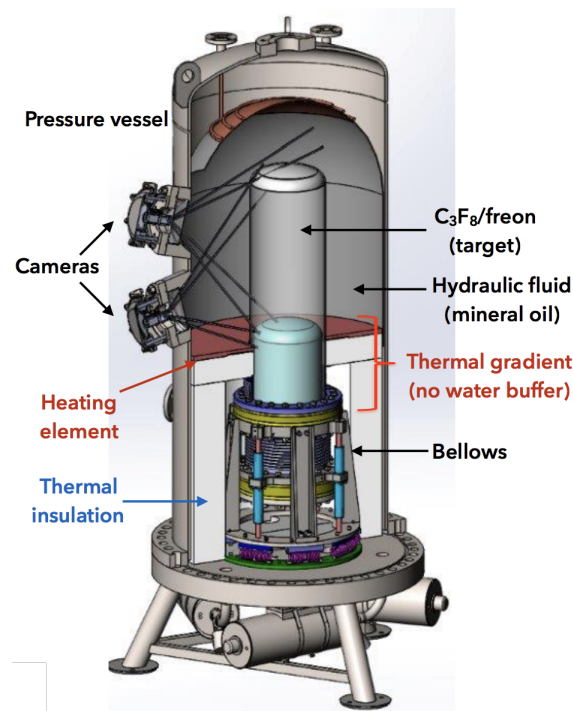
Figure 3.4: PICO-40 bubble chamber.

After PICO-60 second run and its success, PICO collaboration decided to work towards a new project: PICO-40L. This version differs from its predecessor mainly because it eliminates the buffer liquid inside the detector. The buffer liquid was removed after concluding that a large part of the background was originated here. Another background noise were contaminants inside the pressure vessel. It is the first experiment to be constructed using *right-side-up* principle. This principle refers to the orientation given to the bubble chamber. In the previous experiments, as shown in figure 3.3 the bubble chamber's position has the active material facing downwards. In figure 3.4 we can see that the design changed facing it upwards above the thermal gradient; this change is called *right-side-up* principle.

3.2.2 Nucleation Efficiency

As aforementioned, a critical energy is needed to determine an energy limit at which to expect bubble formation with the desired energy deposition. But this transition is not 100% certain even within these conditions [48]. The probability of bubble nucleation for carbon and fluorine as a function of nuclear recoil was determined in previous experiments from the collaboration. The fit was carried out with different efficiency curves using rising linear functions by intervals for each threshold energy. This led to a model for different independent efficiencies for carbon and fluorine at a fixed threshold energy that cannot be determined with Seitz Theory [49].
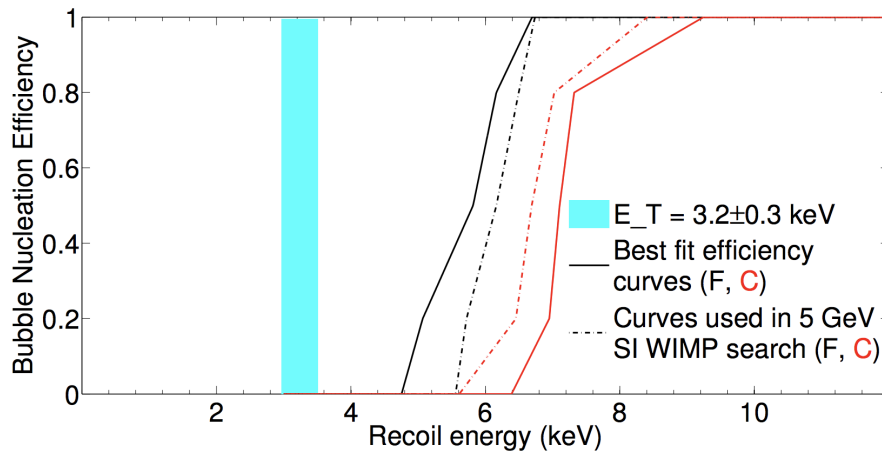
Figure 3.5: Best fits for fluorine (black) and carbon (red) efficiency curves for an energy threshold of 3.2 keV shown in a blue band calculated according to Seitz theory.

The energy that generates the bubble is that of the nuclear recoil. This process depends on the temperature and pressure. If the energy is greater than that of the recoil there should be a 100% efficiency in the bubble formation. But this is not the case. Energies smaller than that of the threshold (E) are designated so that the efficiency is zero. Then

$$eff = a + \left[\frac{E - \epsilon_i}{\epsilon_{i+1} - \epsilon_i} \right] a \tag{3.4}$$

Where a is a value within the $(0, 0.8)$ range in the bubble nucleation efficiency, and it depends on ϵ_i. Equation (3.4) is a line, therefore it is possible to use lines to deduce their initial and final energies in experiments. FermiLab, a highe energy physics laboratory, carried on this calculations to predict the lines' parameters and ended up with the result shown in Figure 3.3.

3.2.3 Bubble Chamber Operation

As described before when above the critical energy, energy is deposited in the active material of the detector and a bubble is formed. The cameras and acoustic sensors

take data on the bubble formation. After some milliseconds, the growing of the bubble is stopped by increasing the pressure [48]. The compression takes place for some minutes and the whole procedure starts again.

The main idea of the detection process in the PICO experiments rely on an energy threshold that, while being satisfied according to Seitz criteria, will trigger a change of phase; thus a bubble will emerge. This method however is not unerring and to account for its accuracy, the detector's response probability has to be studied.

The experiment's target is mainly fluorine nuclei with odd total angular momentum. The design is very sensitive to WIMP-proton spin-dependent interactions; thus, one of the most promising candidates is ^{19}F because its spin is associated to the non-coupled proton which makes for a bigger cross-section in comparison to other nuclei.

3.2.4 PICO 500

PICO-500 is a project that is in its design phase. The experiment is expected to be the biggest of its kind as it will have a tank of at least 500 litres. The experiment, as its predecessors, is extremely sensitive to spin-dependent interactions between WIMPs and protons. Nuclei with odd angular momenta are needed to search for spin-dependent coupling. This can be found in CF_3I and C_3F_8 substances. C_3F_8 was used for PICO-40 and PICO-60 *run 2*, now it is being considered in early design models for PICO 500.
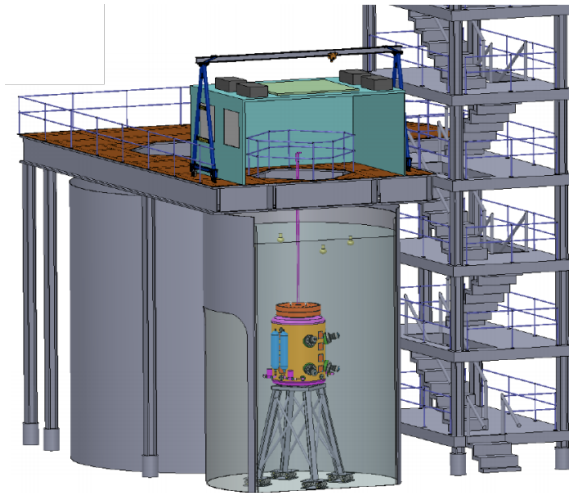
Figure 3.6: PICO-500 model beside DEAP-360 tank below the control deck.

At this stage, the stainless steel pressure vessel has not fixed dimensions. The simulations were carried out using two different models with different radii and height. So far, the detector construction code remains unfinished. The simulations being carried out help motivate design decisions. Final dimension and material choice criteria

is being developed in this stage. This work will guide the design of the detector by providing simulation data of the different available geometries for the pressure vessel and the quartz jar. Additionally, the simulation process also considers new components (reflector, base, acoustic piezos, cameras, base, etc.) in the GEANT4 code. Some parts of the detector where built and added considering the different sizes the pressure vessel and quartz jar can have. Specific simulations were carried out for each of the added experiment's parts, such as the base and cameras, for the ^{232}Th and ^{238}U decay chains. The simulations were carried twice since we considered two models with different dimensions. There were four models and the ones with the biggest amount of active material were chosen for the simulations.

Chapter 4

Background

Direct detection techniques face the problem of singling out weak, small signals among a surplus of background signals that come from different sources. The ongoing astro-particle physics experiments have to deal with discrimination processes in the received signals that are considered in the design process as well as in the analysis. The current limits, as in super symmetric propositions of dark matter particles, expect less than a single event per tonne of material per year. To be sure of possible positive results in the bubble chamber it is very important to identify and characterize all possible nucleations generated by ordinary matter.

4.1 Neutrons

The signals produced by neutrons are the hardest to discriminate and characterize since they are very similar to the expected nuclear recoil of a WIMP. It is a very important part of the direct detection process. This kind of background comes mainly from fission and (α, n) reactions produced by decays of ^{238}U, ^{235}U and ^{232}Th present in the materials that constitute the experiment. Cosmic Ray induced neutrons also have to be taken into consideration, as they contribute greatly to the background. Both types of neutrons can be characterized by their origin: radiogenic or cosmogenic [51].

4.1.1 Radiogenic Neutrons

- *(α,n) Reactions*
  When a radioisotope decays, it typically starts with α particles that try to surpass a nucleus' Coulomb potential

  $$V = k \frac{2Ze^2}{r_0 A^{1/3} + r_\alpha}. \tag{4.1}$$

  Here k is the Coulomb constant, Ze the nuclear charge, $r_0 A^{1/3} \sim r_N$, the nuclear radius, and $r_\alpha \approx 2.3$ fm is the α radius, while the α charge is 2e. At first order, the α-particle will be able to interact with the nucleus if its kinetic energy

surpasses the potential, if the interaction is sufficiently exothermic an α could tunnel through the potential barrier. With enough exothermic energy, the α particle could scatter directly with a nucleus and detach a neutron. However, the energy needed for this to take place is below the scales emitted by the U and Th chains, here, the particles dissolve originating an intermediate neutron. Its energy thermalizes quickly, producing an energetic distribution on all the nucleus components on which the α acts. Intermediate nuclei are usually in an unstable excited state. This energetic state usually covers a continuous energy spectrum. It regularly decays into lower energetic levels and emits a γ, a proton, a neutron, a β, etc.

Energy levels, spin, the excited nucleus's state's parity and the accessibly states for the new nuclei dictate the probability of a neutron being emitted. This calculation considers the intrinsic nuclear physics playing in the material that interacts with the α-particles and their energy spectrum. An important step for this is getting to know the rate concentration for the radioisotopes and the exact composition of the detector's parts.

There are two main software tools to estimate (α,n) reaction in light nuclei: SOURCES-4C and NeuCBOT. Both calculate the (α, n) neutron production. In further chapters, the results gathered by using NeuCBOT code are presented.

- *Environmental Neutrons (α, n)*
  They originate in the radioactive substances that surround the detector. Radon is an important source; the average concentration measured in SNOLAB in April 2016 is 131.0 ± 6.7 Bq/m^3. This way they do not interact as much with the active material within the quartz jar. However, the interactions produced by environmental neutrons, even though they are not as many, are not negligible. Further attempts to analyze this background are needed. Montecarlo simulations in GEANT4 aim to describe an event rate caused by these interactions [52].

- *Spontaneous Fission Neutrons*
  They come from the spontaneous fission reactions in the radioisotopic traces from the materials that shape the detector, 238U and 232Th. For this reason the materials are carefully selected before the detector's construction and go through a thorough inspection in which the event rate, radioisotopic trace concentrations and exact composition of the materials are tested. The spontaneous fission impact in the experiment is about the same than that of (α, n) processes from single neutrons, regardless of it being produced at a rate significantly lower than 1 per α-interaction.
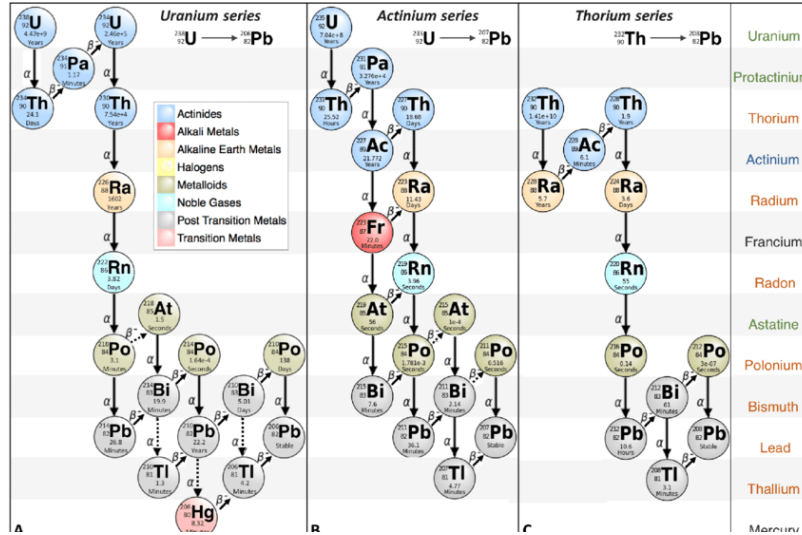
Figure 4.1: Decay chains for U^{238}, U^{235} and Th^{232}.

Radiogenic neutrons are a source of background. To minimize its occurrence there is a material selection, but they still constitute an obstacle to achieve a good sensitive range and to acquire reliable dark matter information from direct detection projects.

4.1.2   Cosmogenic neutrons

Theses neutrons are originated by the cosmic rays, mainly muons, from outer space and the hadronic cascades in Earth's atmosphere. Highly energetic muons become the part of cosmic rays that reach further due to their relatively short half-life and small cross-section [53]. This can be explained by Einstein's time dilation; the muons are created at an altitude of around 15 km and the lifetime of the muons is approximately t= 2.2×10^{-6}s. However, since muons move at such a great speed they are able to reach Earth surface because of time dilation or length contraction. They are able to pass through large rocks which is why direct detection experiments have to be carried out in underground facilities. At SNOLAB, the muon factor reduces to 5×10^7 to that of the surface [54]. The cosmogenic neutrons have several possible sources:

- *Muon Spallation*
  During the ultaenergetic interactions, the muon-nucleus exchange a virtual photon that enables the creation of secondary particles. These particles can be hadrons, such as neutrons, that are the product of spallation processes.
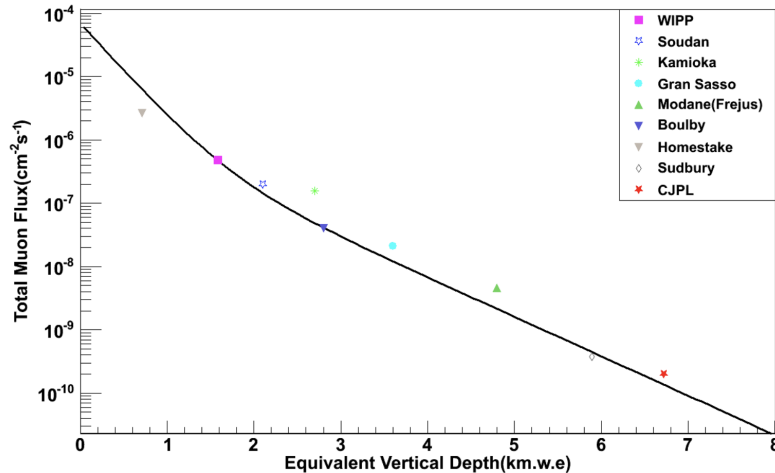
Figure 4.2: Muon flux vs. the depth of different underground laboratories in the world [55].

- *Hadronic Cascades*
  The cosmic ray hadronic cascade can include ultraenergetic neutrons produced in π^- interactions that collide with target nuclei with high proton content. An excited nucleus can be generated and from this, low energy neutrons can be formed.

- *Electromagnetic Cascades*
  Photonuclear reactions produce this kind of nucleus. Muons initiate the electromagnetic cascades during their radiative processes such as Bremsstrahlung radiation in muons, production of muon pairs and muon-nucleus interactions [56]; in turn, the cascades create photons. Generally, (γ, n) reactions take place through giant dipolar resonance present in most nucleus within the energy range of 10-30 MeV.

The neutron flux estimation in the PICO experiments comes from the measurements done for the cavern of the SNO+ experiment. Calculations were done using GEANT4 software. Additionally, the data gathered by the simulations helped evaluate the expected events and provided information for the calculations. Further data recollection by simulations is a key part in the process of designing and modifying these experiments.

4.2 α-Particles

Alpha particles are an important source of background. They are products in the disintegration chains for ^{238}U, ^{235}U and ^{232}Th, however, a big contribution comes from ^{222}Rn which originates from the ^{238}U. The discrimination process for this kind of background had been initially developed by the PICASSO collaboration through

the acoustic detection system [57]. With this, the nuclear recoils can be distinguished from α decays.

4.3 γ-Radiation

Isotopes in the detector's materials, such as ^{238}U, ^{232}Th and ^{40}K , emit gamma radiation. They are able to interact with the active material by Compton scattering. At certain energy thresholds, electron can undergo a ionization process that can produce a nucleation. This problem is handled by ongoing Montecarlo simulations that would predict an event rate that can be taken into consideration for further detector activity. For muons, beta radiation or x-ray interactions, the bubble nucleation can turn negligible by controlling the temperature and pressure [49].

4.4   Neutrinos

Neutrinos are a hard background to discriminate or to tell apart from other signal sources. Neutrinos have several possible kinds of sources. Solar neutrinos are mostly created by the pp solar reactions; they are more common and, even though their energy range is small, they have a high flux and thus contribute highly to the electronic background via neutrino-electron dispersion. Atmospheric neutrinos and supernova diffused neutrinos are considered to have an event rate of 1 to 5 events per 100 times year in dark matter searches below 10^{-48} cm^2 [39, 58]. The neutrino flux is mainly a combination of solar, atmospheric and supernova diffusion neutrinos [49].

4.5   Anomalous Noises

The bubble chamber's cameras metastability can induce nucleations due to surface phenomena [59]. The irregularites in the surface can hold gases that can contribute to the super-heated liquid's evaporation and thus produce a change of phase without any particle interaction. To counteract this effect, the following techniques are employed:

- To have some control over the phase in the boundary between fluids a layer of a liquid (water) is used. This creates an extremely smooth coat that acts as a shock absorber and a cap on the super-heated liquid.

- The active material's container has a small α emission that makes small contribution to the total background. It is made of synthetic silica; it has little imperfections in its inner surface that are removed in the laboratory to ensure a small number of interactions taking place there.

- The accuracy needed in the experiments calls for a high cleanliness level that can be achieved by using a good filtering system in the active material that removes any kind of microscopic dust particles that could trigger additional backgrounds.

Chapter 5

Simulations and Analysis

In the detector it is unavoidable to come across background noises since there is no way to completely suppress them or cancel them. It is possible to identify them and apply certain techniques to still achieve a good level of sensitivity. With the Monte-carlo simulations it is possible to predict the energy distribution entering the active volume and have an overview of the experiment's behaviour. PICO-500's dimensions and the position of its components are yet to be determined. The results of this study will participate in the decision making of these aspects of the experiment. The design specifics will be the product of thorough studies, semi-analytical calculations and Montecarlo techniques.

The designing process includes the evaluation of material selection for each of the components and their geometry. The composition of the materials is specified in NueCBOT for the neutron energy spectra, it is also contained in GEANT4. Additionally GEANT4 has the geometry information. With the material and geometry information the number of expected events due to nuclear recoils is evaluated; from this, an upper and lower bound of background can be contemplated. By considering this number of expected events, the number of potential signals that could mimic the WIMP behaviour is appraised considering its two main sources, ^{238}U and ^{232}Th decay chains.

5.1   Neutron yield in (α, n) reactions

The calculations needed for this can be completed with several different computer codes. The ones used for PICO experiments are NeuCBOT, that uses Talys coding, and SOURCES-4C. SOURCES-4C has helped with dark matter detectors and is well established in previous experimental procedures. NeuCBOT includes more up-to-date nuclear cross sections and works by calculating (α,n) yields and neutron energy spectra for materials that can be constructed within the code and α-particles of any energy. Its functioning combines Talys' calculations, the stopping power of α particles in matter and isotopic decay data.

5.1.1 Nuclear reaction computer codes

SOURCES-4C was developed at Los Alamos Lab and released in 2002. This computer code considers radionuclides decay to determine neutron production rates and spectra from (α,n) reactions, spontaneous fission and delayed neutron emission. The results are based on a 1981 report; since then, a lot of the underlying data has been modified such as the atomic masses, α-decay rates, (α,n) cross-sections and α stopping powers. At this point, new technology has created an opportunity for re-evaluation processes to increase measurement accuracy and new values are now considered.

On the other hand, Talys reaction program was created in 2015 by the Nuclear Research and Consultancy Group and the Atomic Energy Commission. It has the capacity to simulate nuclear reactions that involve neutrons, photons, α-particles, protons, deuterons, tritons and ^{3}He in the 1 keV to 200 keV energy range. It is able to acknowledge a wide variety of nuclear reaction models into a single code NeuCBOT (Neutron Calculator Based on Talys)[64]. This tool is specialized in calculating (α,n) yields and neutron energy sprectra in the range from 0.1 to 15 MeV. Talys is the database that generates the calculations necessary for nuclear reactions and takes information such as the cross-section for the (α, n) reaction between each α-particle. It works by considering the composition of a material that can be created in the material repertoire with specific characteristics that enables the user to fix the material's description per element percentage and the element's isotopes; this information acts as an input. This material is under α-exposure and α-energies described in the lists within the data base. All α-particles have an emission probability included in NeuCBOT libraries. Within NeuCBOT, secular equilibrium for the chains and natural isotopical abundance for each participating element in the material's composition is considered. In gathering all the data data and calculating the weighted sum of the contributions from different α-particles and material elements, an output is generated. It computes the neutron yield as,

$$Y(E_n, E_\alpha) = \sigma(E_\alpha, E_n)\mu. \tag{5.1}$$

Here μ is the number density of the emitter isotope and E_n is the energy of the outgoing neutron. For the α-particles coming from the radioactive decay, we have to consider a lower energy than that of E_α due to the energy loss they suffer while passing through different materials. This correction can be done by considering the stopping power of the material. Additionally, NeuCBOT considers the total yield spectrum chain of radionuclides to calculate the yield.

There are libraries used in NeuCBOT with the emission probability of all the α-particles so that the output spectrum is calculated as a sum of contributions from different α-particles and material elements. This weighted sum considers secular equilibrium for the chains and natural isotopical abundance for each element. However, NeuCBOT does not consider spontaneous fission; in order to take it into account an extra yield from spontaneous fission was added to the (α,n) yields. With the resulting sum the calculations were carried out.

5.1.2 GEANT4

GEANT4 stands for GEometry ANd Tracking. It is a Montecarlo simulation tool to model the path of particles through matter. This program is usually used in high energy physics, nuclear physics, colliders, medical and space sciences. Its content is an international collaboration who maintains it and updates it [62]. The code is C++ based, it works with different parts that interlink by defining an inter-phase independently. This develops modules that enable the user to methodically modify even the slightest details of the simulation. This also forces the user to make sure everything is defined before running a simulation, since nothing is predetermined. This can make everything really specific, but also requires a vast knowledge of the processes taking place in the simulations. The parameters are incorporated by C++ code, which incorporates basic abstract classes from the GEANT4 scheme. These classes are:

- **G4VUserPhysicsList**
  A *process* includes all kinds of physical systems, like the photoelectric effect, ionization or an elastic dispersion. Whilst a *model* is the description of said process. Every model and process should be orderly placed in the *physics list* of this class to be considered in the simulation.

- **G4VUserDetectorConstruction**
  The geometry and volumes used in the simulations are defined in this class. Here the elements, compounds and mixes, from which the detector is made of, are established and described.

- **G4VUserPrimaryGeneratorAction**
  In this class the main characteristics of the simulated particles used as projectiles in the detector are outlined. This covers their position, momentum and energy. GEANT4 uses the concept of *hit*, that comes from the *G4Hit* class. The hits are used to recompile the simulation's data; the information within the *hit* includes energy deposition, momentum, time and position. In the assigned sensitive volumes by *G4VSensitiveDetector*, are processed or saved at the end of each event in a derivative class of *G4VUserEventAction*.

These simulations are usually carried out with *runs*. A *run* is a sequence of *events*; an *event* is the simulation of one or more primary particles and all the subsequent secondary ones. Primary particles are generated by a particle source at a certain position in space in time zero at the beginning of the event. The particles are then moved by *steps* through the simulated geometry. The steps are determined by the physical processes involved. All the created particles are registered and recorded until their energy is zero, until they disappear by some reaction or until they leave the simulated volume limit (a.k.a. World Volume). If the particles deposit energy in the sensitive volume of the detector, after each step the simulation will record the information of the deposited energy up to the end of the event. Later, the data can be either analyzed or saved permanently.

5.2 Experiment Design

The work was divided in several stages. Since PICO500 is in its development phase, there are many decisions yet to be made. For this a lot of studies have to take place to try to chose the best available options. The first stage of the GEANT4 layout consisted of the cubehall inside of one of SNOLAB's caverns. Once inside, one can find two water tanks, one of which hosts the DEAP360 experiment, beside it, the simulation shows a second tank that holds the next PICO experiment.

The design for PICO500 is still in its early stages, therefore the visualization is simple and lacks many components. Inside the water tank, you can find a pressure vessel filled with mineral oil in which the quartz jar is submerged. The quartz jar is the container for the active material, C_3F_8.
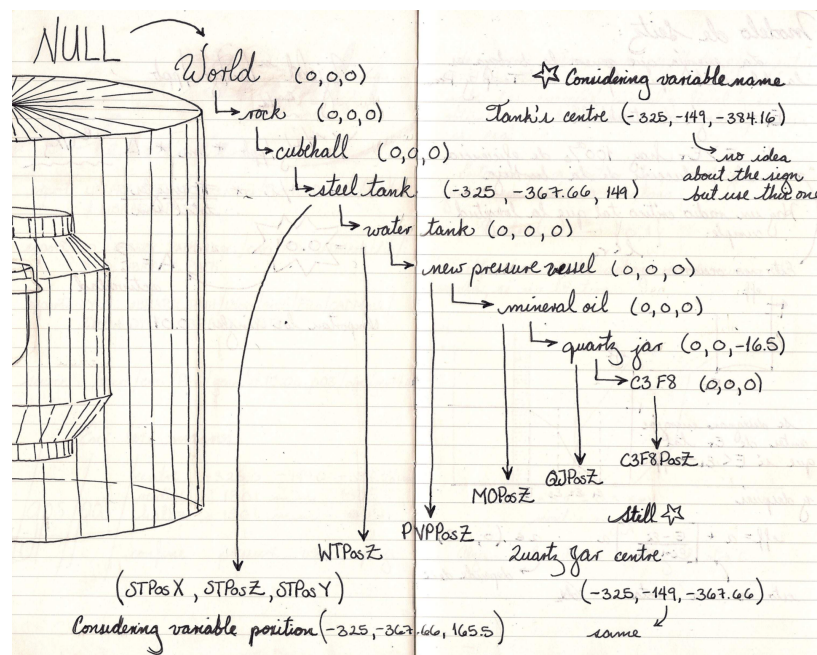
Figure 5.1: Early design for the PICO500 model showing the centre coordinates for each of the components and their mother volume used in GEANT4.

The rudimentary design, shown in figure 5.1 was the initial point for the current work. From here there were two possible options for the two components. There are two dimension options for the pressure vessel and two for the quartz jar. By mixing them and trying the different combinations we ended up having four models.

5.2.1 General Models

Pressure Vessel Dimensions

- *Option 1*:
  outer diameter=213.4 cm
  height=365.8 cm
  shell thickness=5.1 cm
  mass=12361.4 kg

- *Option 2*:
  outer diameter=152.4 cm
  height=335.3 cm
  shell thickness=3.8 cm
  mass=5773.7 kg

Quartz Jar Dimensions

- *Option 1*:
  radius=22.9 cm
  height=172.7 cm
  mass=309.4 kg

- *Option 2*:
  radius=38.1 cm
  height=223.5 cm
  mass=1403.4 kg

There were some simulations conducted on the four possible models built from this. The first model was that of the Pressure Vessel option 1 and the Quartz Jar option 2 as can be seen in figure 5.2. The second was PV1 and QJ2, the third PV2 and QJ1 and finally the fourth PV2 with QJ2, shown in figure 5.3. Several simulations were carried out for the Thorium^{232} and Uranium^{238} chains in 316 L Stainless Steel. With this, the permitted activity could be calculated by establishing 0.01 single events per year per chain. The number of multiple and single events could be counted with the program ROOT using a script[1]. However this first simulations were not conclusive since the statistics involved were not enough. In the first try for each model 5×10^8 was the average number of simulated events, and still, the resulting single events counted were less than a hundred. This showed that more statistics are needed. Another round of simulations was carried out with bigger computational resources using Compute Canada [64]. These results are shown later on.

For the next step, to simulate the most relevant internal components, such as the cameras, acoustic transducers, retro-reflector and illumination system, the models with the largest mass of active material were chosen; being Model 2 and Model 4, which have the same quartz jar dimensions and defer only in the pressure vessel size.

---

[1]See Appendix A.
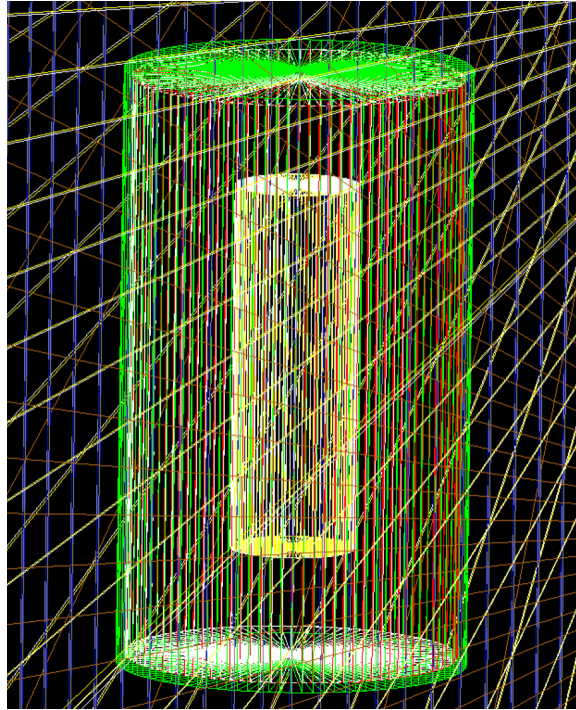
Figure 5.2: Model 2, pressure vessel option 1 with a mass of 12361.4 kg, and quartz jar option 2, with a mass of 1403.4 kg.
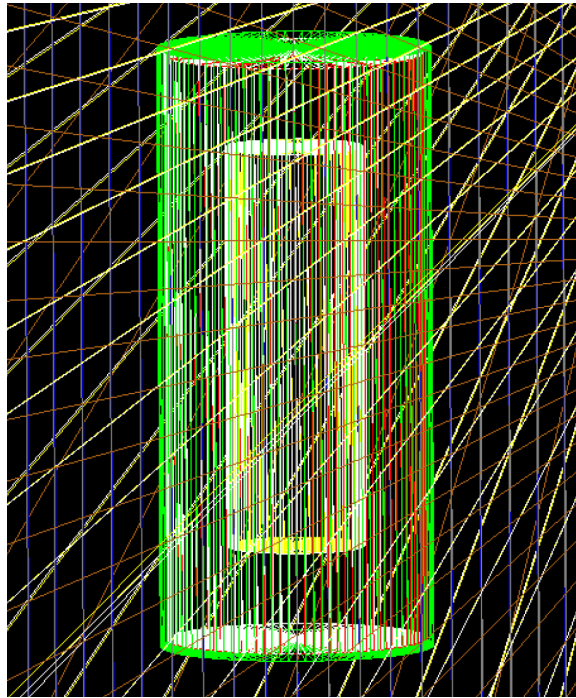
Figure 5.3: Model 4, pressure vessel option 2 with a mass of 5773.7kg, and quartz jar option 2 with a mass of 1403.4 kg.

5.2.2 Component Introduction

The most important internal components were added to the main structure of both relevant models in the GEANT4 Detector Construction. These additions are the detector's parts for which simulations were later carried out to collect data on their contribution to background. By doing this, we can estimate the number of events each of the components cause, and furthermore take preventive measures or design decisions to choose the most convenient materials and size options for the general purpose.

The added components are:

- *base*
  This is a polyethylene cylinder in the bottom part of the detector. It is inside the pressure vessel and it covers the volume below the quartz jar. It acts as a thermal insulator.

- *LED*
  In the simulations the LEDs are positioned as a cylinder at the middle outside of the pressure vessel. Its composition is mainly aluminum but it is considered only for the energy spectrum. The detector construction in GEANT4 simulates it as an air cylinder. Their purpose is to provide illumination for the cameras.

- *PCB*
  Same as the LED, the position is considered to be at the outside middle part of the pressure vessel as an air cylinder. PCB stands for printed circuit board, this component contains the means to monitor the part of the experiment.

- *camera*
  Same as the LED and PCB, the position is considered to be at the outside middle part of the pressure vessel as an air cylinder. This video camera is in charge of taking pictures and video of the bubble formation.

- *piezos*
  There are two of this components. Both of them are inside the pressure vessel next to the quartz jar. The first one is at the middle of the jar and the second is at the bottom limit of it. Both of them are acoustic sensors. The sound made during the bubble formation is part of the data collected during the experiment.

- *reflector*
  The reflector is a this surface covering the inner walls of the pressure vessel and covering only the quartz jar height. Its function is to provide more light in the active material region to aid the cameras take pictures.
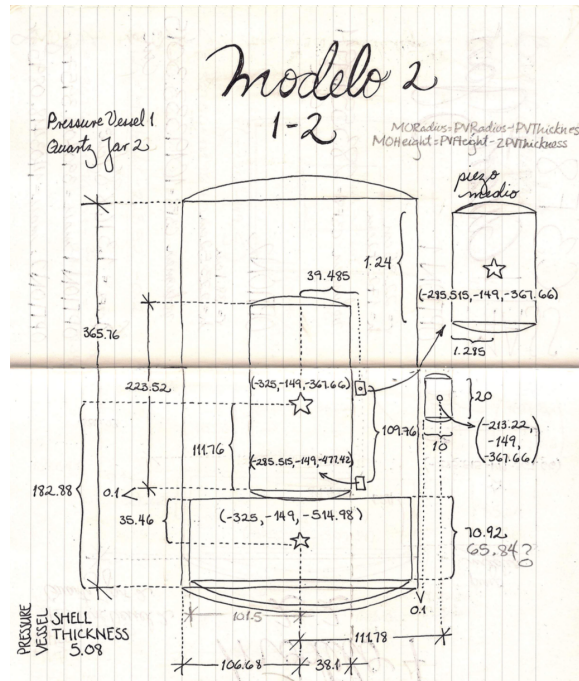
Figure 5.4: Model 2. Components diagram with centres and dimensions.
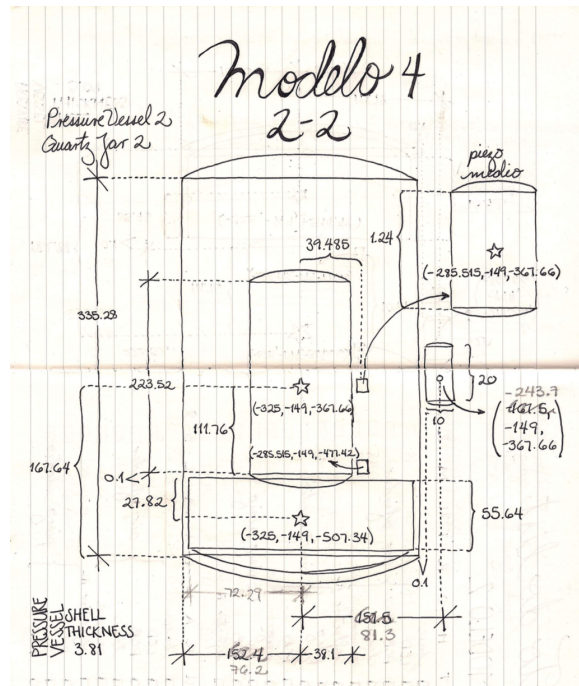
Figure 5.5: Model 4. Components diagram with centres and dimensions.

These components were added to the geometry layout and several simulations took place. In this step it was important to determine the location for each of them in the general frame of reference and in the local one when considering mother volumes.

The Mother volumes are used in the GEANT4 code and are essential for the geometry development. The diagrams used for the geometric buildup are shown in figure 5.4 and figure 5.5. We estimated their contribution in the number of events per year and a sum was made to estimate the number of events caused by material selection and geometric characteristics. Further more by fixing the desired contribution we can calculate the permitted activity per material and decay chain permitted to get the target limit. This limit is set to be 0.01 per chain per element.

Some of this components such as the *piezos* are composed by more than one part. For the simulations a different macro was used to include the PCB, copper and piezo part.

5.2.3 Radiopurity

The amount of ^{232}Th, ^{235}U and ^{238}U in each of the components can be determined by spectroscopy techniques from the gamma emission in radiopurity labs at SNOLAB and the University of Chicago. A high purity germanium detector is used in this process, while in a cryogenic environment, to detect the emitted photons [60].

5.2.4 Simulations

Previous work is gathered to simulate the neutron production. The main software used are SOURCES-4c and NeuCBOT, for this project NeuCBOT was selected. The process consisted in finding the neutron yield and its energy spectrum for each of the materials added in the simulation. This was done considering their element composition and radioisotope abundance. With this at hand, the next step is a GEANT4 simulation.

Montecarlo methods are based in random numbers and probability, they are an alternative manoeuvre to turn to when analytical methods are too complicated or impossible to carry out [61]. It has several advantages since these methods can be performed even when there's not a lot of information available. The initial precise value of the model's parameters can be unknown or be represented by probability distributions. This attributions make Montecarlo simulations a good candidate to model the interaction between different kinds of particles and ordinary matter. In this process, the simulation starts by randomly choosing the primary particles considering their momentum distribution and energy, then they are emitted and gradually move through the geometry. In each phase of the simulation process the physical aspects are implemented based on their probability to happen. The qualitative aspect of how many particles interact with the detector is possible to know, as well as other physical properties such as energy and momentum.

PICO500 Geometry

G4VUserDetectorConstruction is an abstract class, used to handle the model's geometry for the simulation. This is carried out by developing a computational code. This code uses solids as separated entities to describe the different volumes that make up the detector. Solids are simple geometrical figures that can be described with certain parameters. These figures can be parallelepipeds, trapezoids, conical sections and cylindrical; they are built following the concept of Constructive Solid Geometry (CSG) [62].

The detector's geometrical layout is usually more complex than that of simple figures. More complex figures can be defined in the simulation's geometry, however, this is an arduous task since the parameters and the space dimensions should be thoroughly known. This is a tricky criteria call, since geometry inaccuracies can have a huge impact in the simulation's results. Therefore, in this stage most of the detector's parts are described as an ensembles of multiple simple figures that combine into more complex systems. Other collaborations work by merging GEANT4 with other tools that makes it possible to introduce more convoluted geometries for the simulation. This processes usually have to be introduced into GEANT4 with GDML (Geometry Description Markup Language) by intermediate conversions to import their models. This way, physical aspects such as material properties and setups can be kept. Yet, this cannot always be done.

For PICO500 geometry the layout was described by using simple geometrical figures exclusively. By combining them and describing them as an ensemble they could be considered as more complex models of the detector's components. Further merging with other computational tools was not considered since the simulations carried out were just a background inquest.

5.3 Results

The study of background is truly important. Since we are working with detection experiments that aim to find unlikely events such as the elastic dispersion of a WIMP with an atomic nucleus, it is crucial to understand and characterize the role they play in the simulations. If the event rate due to background is too high then it becomes impossible to carry out a dark matter detection experiment. It's impossible to ensure a null background, and even if a very low background is achieved, it is important to quantify it correctly. A miscalculation can lead to signal misinterpretations, and then, statistical significance cannot be ascribed to any excess over the total event rate.

PICO500's candidates differ in dimensions only, whereas the main function idea of the detector remains the same. Thus, its components and materials are the same. A simulation for each of them was carried out to compare the different possible designs. For describing the next results the models were named after the option of pressure

vessel and quartz jar that were considered. Then *Modelo1-1* refers to pressure vessel option 1 and quartz jar option 1; Then *Modelo1-2* refers to pressure vessel option 1 and quartz jar option 2 and so on. The results are as follow:

Model	^{232}Th		^{238}U	
	Singles	Multiples	Singles	Multiples
Model 1-1	17	124	24	87
Model 1-2	183	1057	110	610
Model 2-1	1857	10865	1371	7933
Model 2-2	1852	10885	17786	122134

Table 5.1: Simulation results for different models.

The statistics used in each of the simulation varies. There was a low number of counted bubbles in the initial simulations with 5E6 simulated events. The number of simulated events had to be increased to reach a significant result. Events were added to the initial considered number to reach more conclusive data.

Model	PV mass $\left[kg\right]$	QJ mass $\left[kg\right]$	# simulated events	Activity $\left[\frac{mBq}{kg}\right]$	
				^{232}Th	^{238}U
Model 1-1	12361.4	309.4	7.25×10^9	5940	4950
Model 1-2	12361.4	1403.4	4.24×10^9	323	297
Model 2-1	5773.7	309.4	5.00×10^9	80.2	124
Model 2-2	5773.7	1403.4	5.00×10^9	40.2	4.77

Table 5.2: Simulation's description for the ^{232}Th and ^{238}U decay chains.

The PICO collaboration had developed several discrimination techniques throughout their multiple different experiments. These also aim to reduce the electromagnetic and α-particles background. Neutron originated background, however, needs other processes to be analyzed. This case is really difficult to reduce or discriminate due to its nature. Thus, complex procedures need to be implemented to deal with this kind of background. Montecarlo simulations carried out with GEANT4 can describe and characterize its behavior within the detection process. The number of events per year per components is set to be 0.01 so that the experiment's total adds up to less than 0.1. The maximum activity allowed for this limit is displayed in table 5.2. The simulations' results can be compared with the data gathered in previous experiments and establish a prediction rate. Montecarlo's prediction is set side by side with the number of single and multiple events counted in previous experiments. The prediction can also be carried out beforehand to help design the simulated detector. This data can help decide certain characteristics for the future detector, such as the materials and the dimensions of its components. With this goal in mind, the mentioned additions were made to the geometry and with them further simulations were carried out.

The models with the biggest amount of active material were chosen to be compared with the added components.

Model 1-2	^{232}Th		^{238}U	
	Singles	Multiples	Singles	Multiples
base	2186	11375	2381	12030
PCB	<1	<1	<1	<1
LED	<1	<1	<1	<1
lenses	<1	<1	<1	<1
camera	<1	<1	<1	<1
TitaniumReflector	3	15	<1	<1
AluminumReflector	<1	<1	<1	<1
MiddlePiezo	6772	43869	6475	42871
MiddlePiezo : *Copper*	6564	36319	6541	36420
MiddlePiezo : *PCB*	7057	45136	7488	46135
LowerPiezo	6972	28658	6741	27793
LowerPiezo : *Copper*	6773	24551	6623	23889
LowerPiezo : *PCB*	7130	29223	7201	30249

Table 5.3: Simulation results per component and decay chain for Model 1-2.

Model 2-2	^{232}Th		^{238}U	
	Singles	Multiples	Singles	Multiples
base	6705	32153	6969	34947
PCB	41	289	26	218
LED	38	238	25	178
lenses	44	309	28	228
camera	53	323	18	252
TitaniumReflector	283	2002	235	1453
AluminumReflector	152	958	96	66
MiddlePiezo	6813	44081	6466	42525
MiddlePiezo : *Copper*	6345	36337	6311	35735
MiddlePiezo : *PCB*	7176	44769	7500	46208
LowerPiezo	7000	29273	6803	28325
LowerPiezo : *Copper*	6828	24385	6604	23879
LowerPiezo : *PCB*	7038	29278	7327	29819

Table 5.4: Simulation results per component and decay chain for Model 2-2 with 5E6 simulated events.

The data obtained with this was sufficient to count the number of single and multiple bubbles produced in the detector.

Model 1-2

	mass $\left[kg\right]$	# simulated events	Activity $\left[\frac{mBq}{kg}\right]$	
			^{232}Th	^{238}U
base	2754.4	$5.00{\times}10^{6}$	$1.43{\times}10^{-1}$	$1.49{\times}10^{-1}$
PCB	$5.00{\times}10^{-2}$	$5.00{\times}10^{6}$	$5.43{\times}10^{11}$	$6.21{\times}10^{11}$
LED	$1.14{\times}10^{-1}$	$5.00{\times}10^{6}$	$2.37{\times}10^{11}$	$2.71{\times}10^{11}$
lenses	$5.55{\times}10^{-2}$	$5.00{\times}10^{6}$	$4.89{\times}10^{11}$	$5.59{\times}10^{11}$
cameras	$7.40{\times}10^{-2}$	$5.00{\times}10^{6}$	$3.67{\times}10^{11}$	$4.19{\times}10^{11}$
TitaniumReflector	4.9	$5.00{\times}10^{6}$	$5.81{\times}10^{4}$	$1.12{\times}10^{5}$
AluminumReflector	4.9	$5.00{\times}10^{6}$	$3.02{\times}10^{4}$	$4.68{\times}10^{4}$
MiddlePiezo	$1.20{\times}10^{-3}$	$1.00{\times}10^{5}$	$1.06{\times}10^{5}$	$1.26{\times}10^{5}$
MiddlePiezo : Copper	$2.11{\times}10^{-2}$	$1.00{\times}10^{5}$	$7.10{\times}10^{3}$	4950
MiddlePiezo : PBC	$1.30{\times}10^{-3}$	$1.00{\times}10^{5}$	$1.01{\times}10^{5}$	297
LowerPiezo	$1.20{\times}10^{-3}$	$1.00{\times}10^{5}$	$1.03{\times}10^{5}$	$1.21{\times}10^{5}$
LowerPiezo : Copper	$2.11{\times}10^{-2}$	$1.00{\times}10^{5}$	$7.01{\times}10^{3}$	4950
LowerPiezo : PBC	$1.30{\times}10^{-3}$	$1.00{\times}10^{5}$	$1.05{\times}10^{5}$	297

Table 5.5: Simulation's description per component for model 1-2.

Model 2-2

	mass $\left[kg\right]$	# simulated events	Activity $\left[\frac{mBq}{kg}\right]$	
			^{232}Th	^{238}U
base	2754.43	$5.00{\times}10^{6}$	$4.66{\times}10^{-2}$	$12.8{\times}10^{-2}$
PCB	$5.00{\times}10^{-2}$	$5.00{\times}10^{6}$	$1.32{\times}10^{10}$	$2.38{\times}10^{10}$
LED	$1.14{\times}10^{-1}$	$5.00{\times}10^{6}$	$6.25{\times}10^{9}$	$1.08{\times}10^{10}$
lenses	$5.55{\times}10^{-2}$	$5.00{\times}10^{6}$	$1.11{\times}10^{10}$	$1.99{\times}10^{10}$
cameras	$7.40{\times}10^{-2}$	$5.00{\times}10^{6}$	$6.92{\times}10^{9}$	$2.33{\times}10^{10}$
TitaniumReflector	3.53	$5.00{\times}10^{6}$	838.35	$1.20{\times}10^{3}$
AluminumReflector	3.53	$5.00{\times}10^{6}$	$1.59{\times}10^{3}$	$3.89{\times}10^{3}$
MiddlePiezo	$1.20{\times}10^{-3}$	$1.00{\times}10^{5}$	$1.05{\times}10^{5}$	$1.26{\times}10^{5}$
MiddlePiezo : Copper	$2.11{\times}10^{-2}$	$1.00{\times}10^{5}$	$6.21{\times}10^{3}$	$7.36{\times}10^{3}$
MiddlePiezo : PBC	$1.30{\times}10^{-3}$	$1.00{\times}10^{5}$	$9.22{\times}10^{4}$	$1.00{\times}10^{5}$
LowerPiezo	$1.20{\times}10^{-3}$	$1.00{\times}10^{5}$	$1.02{\times}10^{5}$	$1.20{\times}10^{5}$
LowerPiezo : Copper	$2.11{\times}10^{-2}$	$1.00{\times}10^{5}$	$5.97{\times}10^{3}$	$7.03{\times}10^{3}$
LowerPiezo : PBC	$1.30{\times}10^{-3}$	$1.00{\times}10^{5}$	$9.40{\times}10^{4}$	$1.03{\times}10^{5}$

Table 5.6: Simulation's description per component for model 2-2.

5.4 Conclusions

The decision making for the design of the model will be based on the results shown in the previous tables. In table 5.1, the number of single and multiple bubbles predicted

in the pressure vessel options for each of the models per decay chain is shown. Typical purity of stainless steel for ^{238}U chain is lower than 0.2 ppb which is around 2.47 $\frac{mBq}{kg}$; and for the ^{232}Th chain lower than 1 ppb, equal to 4.07 $\frac{mBq}{kg}$. The results in table 5.2 show that this works with all models because all of them allow a higher activity than the typical values mentioned. All 4 models are good candidates for the design but two models were chosen from table 5.1 due to its mass value. Model 1-2 and model 2-2 are the ones with the biggest amount of C_3F_8, and thus further simulations were carried out taking in mind these dimensions. In table 5.2 we can see that the greatest permitted activity values are from model 1-1. For the rest of the models the activity range is smaller, specially for models 2-1 and 2-2. However, on table 5.3 we can see that for many of the components of the experiment model 1-2 provides less than one bubble per part. For Model 2-2, in table 5.4, the number of bubbles is slightly higher.

With this results, the purity levels needed in the experiment for Model 1-2 is lower and easier to achieve than that of Model 2-2. It shows that the materials used for the detector have a less rigorous margin and thus accept a lower level of purity in the detector's composition.

Since the vale of maximum activity perimitted is high, both models, allow a low level of radiopurity in the materials. The critical part in the models is the polyethylene base. For the base the radiopurity has to be ultra pure at ppt level. The base is the component in which we can find the highest activity as shown in table 5.5 and table 5.6. In model 1-2 for the ^{232}Th chain, the base presents and activity of 0.143 $\frac{mBq}{kg}$=35 ppt and for ^{238}U chain the base has an activity of 0.149 $\frac{mBq}{kg}$=12 ppt. The desired ppt radiopurity level is reached. On the other hand, model 2-2 also complies the same radiopurity level since for the ^{232}Th chain it has an activity of 0.0466 $\frac{mBq}{kg}$=11 ppt and for the ^{238}U chain the activity value is 0.128 $\frac{mBq}{kg}$=10 ppt. These results show that both models have similar radiopurity limits, and thus, considering this aspect, they are equally good design candidates.

The decision concerning the experiment's dimension and development still needs further study. The actual design is still very simple. PICO500 experiment is still at an early development stage, but it forms part of a group of dark matter detectors that have been important in the field of physics beyond the standard model. The PICO projects have pursue the dark matter detection by using the bubble chamber technique. These efforts have been hosted by the underground facility, SNOLAB, in Canada. This laboratory is currently undergoing several experiments in the search of dark matter; however the largest PICO version so far is expected to use approximately a tonne of active material. This experiments is in development and this work focuses on aiding this process.

PICO500 is the next generation detector that will use an improve its predecessors principles and results. Some of its features will remain faithful to the first experiments like PICO60 and PICO40 since all of them share the bubble chamber technique.

However, some improvements are considered; the detector will also use the *right-side-up* concept just like in PICO40L. Now the efforts are focused in the design details for the inner vessel, made of synthetic quartz jar, and the pressure vessel made of stainless steel. The experiment is expected to lead the sensitivity bounds established so far by operating with the largest amount of C_3F_8. The main idea focuses on dark matter coupling to ordinary matter and producing signals in the nuclear recoil process.

As all the previous PICO experiments, PICO500 is to be located at SNOLAB. It has received full funding and permissions from the Canadian authorities. The conceptual design had already started and SNOLAB have already assigned a place for it at the cube hall area of the lab. Here PICO500 will be sharing space with another dark matter detector DEAP-360.

The efforts taking place to detect and prove dark matter are present worldwide. Each of the experiments aim to have high sensitivity levels that are hard to achieve. The projects use different techniques to design the experiments. All of them have to deal with background and ways of minimizing it. All the collaborations work hard to get good data. PICO500 is expected to provide the best results yet to be produced by the PICO collaboration. The PICO bubble chamber technology has provided the best global limits on direct detection of dark matter for WIMP-proton spin dependent cross sections. They work with the best background discrimination techniques in the search for dark matter. The endeavour present had placed them as leading experiments in their field.

Appendices

Appendix A

Root Code to Count Simulation Events

```cpp
//Efficiency nucleation curve for Carbon (MeV).
double effcarbon(double recoil)
{
  double eff;
  if(recoil <= 0.0063889){eff=0.0000;}
  else if(recoil >= 0.0092432){eff=1.000;}
  else if(0.0063889 < recoil <= 0.0069502){eff=0.0000+((recoil
     -0.0063889)/(0.0069502-0.0063889))*(0.2000);}
  else if(0.0069502 < recoil <= 0.0071038){eff=0.2000+((recoil
     -0.0069502)/(0.0071038-0.0069502))*(0.3000);}
  else if(0.0071038 < recoil <= 0.0073202){eff=0.5000+((recoil
     -0.0071038)/(0.0073202-0.0071038))*(0.3000);}
  else if(0.0073202 < recoil <= 0.0092432){eff=0.8000+((recoil
     -0.0073202)/(0.0092432-0.0073202))*(0.2000);}
  return eff;
}

// Efficiency nucleation curve for Fluorine (MeV).
double efffluorine(double recoil)
{
  double eff;
  if(recoil <= 0.0047530){eff=0.0000;}
  else if(recoil >= 0.0066947){eff=1.000;}
  else if(0.0047530 < recoil <= 0.0050678){eff=0.0000+((recoil
     -0.0047530)/(0.0050678-0.0047530))*(0.2000);}
  else if(0.0050678 < recoil <= 0.0058167){eff=0.2000+((recoil
     -0.0050678)/(0.0058167-0.0050678))*(0.3000);}
  else if(0.0058167 < recoil <= 0.0061628){eff=0.5000+((recoil
     -0.0058167)/(0.0061628-0.0058167))*(0.3000);}
  else if(0.0061828 < recoil <= 0.0066947){eff=0.8000+((recoil
     -0.0061628)/(0.0066947-0.0061628))*(0.2000);}
  return eff;
}
```

```cpp
// The void method receive as entries the PICO-60 component name (
    myimput) and the chain (either U238, U235 or Th232) to analyze
void countFromroot(const char * myinput,const char * chain)
{


  // Declaration of a structure to save the component name(
      component), (mass), (neutron yield), )magnitude of the
      radioisotope
  // contamination) and the number of simulated events (simulated)
      .


  struct Info
  {
    string component;
    double mass;
    float neutronyield;
    //double concentration;
    //double uncertainty;
    double result; //AQU  CAMBI  ALGO
    long int simulated;
  };


  // Variables to be used in the structure declared above are
      obtained from the file pico60_(chain).csv
  Info pico500;
  ifstream student;
  char informationfile[1024];
  sprintf(informationfile,"pico500_%s.csv",chain);

  // Declaration of the L (live time of the detector in seconds)
  const long int factor = 31557600;

  //The reading ascii instruction is replaced to read a root file.
  char inputfile[1024];
  sprintf(inputfile,"%s_%s.root",myinput,chain);


  TFile *rootfile= new TFile(inputfile,"READ");
  TTree *tree= (TTree*)rootfile->Get("tree1"); //tree1 neutrons
    are saved  neutrons,
                                  //tree2 gammas are
                                        saved

  // Output file that will contain all the needed information in
      latex style, chiefly those related with the number of events
  // that passed the efficiency curve (bubbles), the rate and
      their multiplicities to 1,2,3,4,5,6 and multiple events.

  ofstream output;
  char outputfile[1024];
  sprintf(outputfile,"%s_%s.txt",myinput,chain);
```

```cpp
// Output file that contains the number of events that passed
    the efficiency curve (bubbles)
ofstream sumbubble;
char sumbubblefile[1024];
sprintf(sumbubblefile,"%s_bubble.out",myinput);

// Output file that contains the rate events
ofstream sumrates;
char sumratesfile[1024];
sprintf(sumratesfile,"%s_rates.out",myinput);

//input.open(inputfile,ios::out);

//Declaracion de variables para leer las "ramas" del tree
Double_t Event;
Double_t VertexX;
Double_t VertexY;
Double_t VertexZ;
Double_t Element;
Double_t Edep;
Double_t Xpos;
Double_t Ypos;
Double_t Zpos;
Double_t ParentID;
Double_t StepN;
Double_t InitE;

//Each branch is associated to the declared variables, no empty
    columns are included.
tree->SetBranchAddress("Event",&Event);
tree->SetBranchAddress("VertexX",&VertexX);
tree->SetBranchAddress("VertexY",&VertexY);
tree->SetBranchAddress("VertexZ",&VertexZ);
tree->SetBranchAddress("Element",&Element);
tree->SetBranchAddress("Edep",&Edep);
tree->SetBranchAddress("Xpos",&Xpos);
tree->SetBranchAddress("Ypos",&Ypos);
tree->SetBranchAddress("Zpos",&Zpos);
tree->SetBranchAddress("ParentID",&ParentID);
tree->SetBranchAddress("StepN",&StepN);
tree->SetBranchAddress("InitE",&InitE);

//These same variables are used to avoid more changes below.
string line;
int event=0;
float empty1=1;
float empty2=1;
float empty3=1;
float empty4=1;
float empty5=1;
float empty6=1;
float empty7=1;
float inter,element,time;
```

```cpp
  float recoil,neutron,initne;
  float x,y,z;


  int index=0;
  int singles=0;
  int multiples=0;
  int event_old=-10;
  const int size=20;
  int bubbli[size];


// Array that save the multiplicity of the events (bubbles)
  for (int m=0;m<size;m++)
  {
    bubbli[m]=0;
  }

  TRandom* r0= new TRandom(0);
  r0->SetSeed(0);

  Int_t entries= tree->GetEntries();
  cout<<"Entries "<<entries<<endl;

  //The cycle is done by the number of entries in the tree.

  for (int i=0; i<entries; i++)
  {
    tree->GetEntry(i);//Access to the tree
//    for (Int_t i=0; i<44;i++){

    event=Event;
    element=Element;
    recoil=Edep;
    x=Xpos;
    y=Ypos;
    z=Xpos;
    neutron=StepN;
    initne=InitE;

    //cout << recoil*1000. << " " << event <<  " " << element <<
        endl;

    // In accordance to the efficiency nucleation curve declared
        at the begginin of the text,
    // only those lines that  fulfill this prerequisit are
        analyzed.
    if (element==6000)
      {
        if (r0->Rndm()>effcarbon(recoil)) continue;
      }
    if (element==9019)
      {
        if (r0->Rndm()>efffluorine(recoil)) continue;
```

```
      }


   // Count how many events (bubbles) were selected.
   if (event==event_old)
     {
        index=index+1;
     }
   if (event!=event_old)
     {
        singles=singles+1;
        for (int p=1; p<size;p++)
          {
             if (index==p) bubbli[p-1]=bubbli[p-1]+1;
          }
        if(index>1)
          multiples=multiples+1;
        index=1;
     }
   event_old=event;
}


student.open(informationfile,ios::out);


// From the file (myimput)_(chain).csv, are extracted (mass),(
   neutron yield), (concentration),(uncertainty) and (simulated
   )


while(!student.eof())
  {
    student >> pico500.component;
    student >> pico500.mass;
    student >> pico500.neutronyield;
    //student >> pico500.concentration; aqu  lo estamos
       cambiando para definir el resultado y obtener la
       actividad permitida para  l
    //student >> pico500.uncertainty;
    student >> pico500.result;
    student >> pico500.simulated;

    if(myinput == pico500.component)
      {

         int realsingles=singles-multiples-1;
         bubbli[0]=realsingles;
         int single_rate=realsingles;
         int multi_rate=multiples;
         int total=multiples+realsingles;
         int double_rate=bubbli[1];
         int triple_rate=bubbli[2];
         int cuadruple_rate=bubbli[3];
```

```
                int quintuple_rate=bubbli[4];
                int sextuple_rate=bubbli[5];
                float simulated_events=pico500.simulated;
                float fraction=single_rate/simulated_events;
                // The neutron fluence and uncertainty associated is
                    calculated here
        //AQUI movi todo para obtener la actividad
                float activity=pico500.result/(pico500.mass*pico500.
                    neutronyield*factor*fraction);
                //float neutron_fluence=pico500.mass*pico500.
                    neutronyield*activity*factor; // AQUI SOLO ESTOY
                    TRATANDO DE RECUPERAR EL NUETRON FLUENCE PARA PODER
                    CONTAR LO QUE SIGUE
        //pico500.mass*pico500.neutronyield*pico60.concentration*
            factor;

                //float totaluncertainty = sqrt((0.01)*(0.  01  ) + (0.1)
                    *(0.1) + (pico500.uncertainty/pico500.concentration)
                    *(pico500.uncertainty/pico500.concentration));



                cout << "
                    ------------------------------------------------------------------------
                    " << endl;
                cout << pico500.mass << " kg" << endl;
                cout << pico500.neutronyield << "  /n/Bq/s/" << endl;
                // cout << pico500.concentration <<" +- "<< pico60.
                    uncertainty << " ppm" << endl;   AQUI CHECA QUE NO
                    NECESITES HACER ESTA LINEA DE CONCENTRATION
                cout << pico500.simulated << " simulated events" << endl
                    ;


                cout << "

                    "<< myinput << "                              " << endl
                    ;
                cout << chain <<"        "<< "Singles" << "            "
                    << "Double" << "        " << "Triple"<<
                "            "<<  "Quads" <<"              " <<"Quints"
                    <<"              " <<"Hexs"<< "            "<<"
                    Multiples" << endl;


                cout << "bubbles" <<"        "<< single_rate << "
                        " << double_rate << "          " <<
                triple_rate << "           "<< cuadruple_rate <<"
                            "<< quintuple_rate <<
                "              " << sextuple_rate <<"           "
                    << multi_rate <<"            " << endl;

                cout << "activity [mBq/Kg]"
                    <<"      "<< setprecision (3) << (activity*1000) <<
```

```
            setprecision (3) <<" +- " << (activity*1000) << endl;

            // setprecision (3) <<"      " << (neutron_fluence)*(
                multi_rate/simulated_events) <<
            //setprecision (3) <<" +- " << (neutron_fluence)*(
                multi_rate/simulated_events) << endl;



        output.open(outputfile,ios::out);


        output << "\\multirow{2}{*}{" << chain << "}" << endl;
        output << "& Bubbles: &" << single_rate << " &" <<
          multi_rate << " & \\\\"  << endl;


        output << "& Activity [mBq/Kg]: & $" <<
          setprecision (3) << (activity*1000) << " \\pm " <<
          setprecision (3) << (activity*1000) << "$" <<" &   $"
            << endl;

          // setprecision (3) << (neutron_fluence)*(multi_rate/
              simulated_events) << " \\pm " <<
          //setprecision (3) << (neutron_fluence)*(multi_rate/
              simulated_events) << "$" << " & \\\\" << endl;
        output << "\\cmidrule(lr){3-3}\\cmidrule(lr){4-8}\\
            cmidrule(lr){9-9}" << endl;
        output.close();


        sumrates.open(sumratesfile,ios::app);
        sumrates << setprecision (3) << (activity)
                 << " +- " << setprecision (3) << (activity) <<
                    endl;

          // << "   " << setprecision (3) << (neutron_fluence)*(
              multi_rate/simulated_events)
          //      << " +- " << setprecision (3) << (
              neutron_fluence)*(multi_rate/simulated_events) <<
              endl;
        sumrates.close();



        sumbubble.open(sumbubblefile,ios::app);
        sumbubble << single_rate << "   " << multi_rate << endl;
        sumbubble.close();

      }
    }
  student.close();
  //input.close();
}
```

Bibliography

[1] S. Dodelso, Modern Cosmology. Amsterdam, Netherlands: Academic Pr, 2003.

[2] E. W. Kolb and M. S. Turner, he Early Universe,ront. Phys., vol. 69, pp. 1547, 1990.

[3] Planck Collaboration. Planck 2015 results. Astronomy and Astrophysics, 594, 10 2016. doi: 10.1051/0004-6361/201525830. URL https://arxiv.org/abs/1502.01589.

[4] F. Zwicky. Republication of: The redshift of extragalactic nebulae. General Relativity and Gravitation, 41(1):207–224, 2009. s10714-008-0707-4.

[5] DarkSide-20k collaboration, Collaborative research: Darkside-20k, INFN-NSF Proposal, 2015.

[6] H. Back and DarkSide-20k Collaboration, DarkSide-20k: A 20 ton Liquid Argon Dark Matter Experiment, Mar. 2016.

[7] M. Milgrom, A Modification of the Newtonian dynamics as a possible alternative to the hidden mass hypothesis, vol. 270, pp. 365370, Jul. 1983.

[8] J. D. Bekenstein, Relativistic gravitation theory for the modified newtonian dynamics paradigm, Phys. Rev. D, vol. 70, p. 083509, Oct 2004. [Online]. Available: https://link.aps.org/doi/10.1103/PhysRevD.70.083509.

[9] E. Felten, Milgrom's revision of Newton's laws - Dynamical and cosmological consequen- ces, vol. 286, pp. 36, Nov. 1984.

[10] C. Alcock, The macho project: Microlensing results from 5.7 years of large magellanic cloud observations, The Astrophysical Journal, vol. 542, no. 1, p. 281, 2000. [Online]. Available: http://stacks.iop.org/0004-637X/542/i=1/a=281.

[11] P. A. R. Ade et al., Planck 2015 results. XIII. Cosmological parameters, Astron. Astrophys., vol. 594, p. A13, 2016.

[12] Marusa; Gonzalez Anthony H.; Markevitch Maxim; Randall Scott W.; Jones Christine; Zaritsky Dennis Clowe, Douglas; Bradac. A direct empirical proof of the existence of dark matter. The Astrophysical Journal, 648, 09 2006. doi: 10.1086/508162.

[13] Julio F.; Evrard August E.; Frenk Carlos S. White, Simon D. M.; Navarro. The baryon content of galaxy clusters: a challenge to cosmological orthodoxy. Nature, 366, 1993. doi: 10.1038/366429a0.

[14] N.; Ford W. K. Jr. Rubin, V. C.; Thonnard. Rotational properties of 21 sc galaxies with a large range of luminosities and radii, from ngc 4605. The Astrophysical Journal, 238, 06 1980. doi: 10.1086/158003.

[15] D.H. Perkins. Particle astrophysics.Physics. Oxford University Press, USA, 0199545456,9780199545452,0199545464,9780199545469.

[16] Arno A. Penzias and Robert Woodrow Wilson. A Measurement of excess antenna temperature at 4080-Mc/s. Astrophys. J., 142:419–421, 1965. doi: 10.1086/148307.

[17] Einstein Albert. "Lens-like action of a star by the deviation of light in the gravitational field". Science, 84(506), 1936.

[18] C. Patrignani et al. Review of Particle Physics. Chin. Phys., C40(10):100001, 2016. doi: 10.1088/1674-1137/40/10/100001. URL http://pdg.lbl.gov/

[19] Jonathan L. Feng. Dark matter candidates from particle physics and methods of detection. Annual Review of Astronomy and Astrophysics, 48, 08 2010. doi: 10.1146/ annurev-astro-082708-101659.

[20] Douglas Clowe, Anthony Gonzalez, and Maxim Markevitch. WeakLensing Mass Reconstruction of the Interacting Cluster 1E 0657558: Direct Evidence for the Existence of Dark Matter. The Astrophysical Journal, 604:596–603, 2004. ISSN 0004-637X. doi: 10.1086/381970.

[21] J.; Mun oz J. A.; Vives-Arias H.; Caldero n-Infante J. Mediavilla, E.; Jime nez-Vicente. Limits on the mass and abundance of primordial black holes from quasar gravitatio- nal microlensing. The Astrophysical Journal, 836, 02 2017. doi: 10.3847/2041-8213/ aa5dab.

[22] Lawrence M. Dodelson, Scott; Widrow. Sterile neutrinos as dark matter. Physical Re- view Letters, 72, 1 1994. doi: 10.1103/PhysRevLett.72.17.

[23] M.G.; et al. IceCube Collaboration Aartsen. Searches for sterile neutrinos with the ice- cube detector. Physical Review Letters, 117, 8 2016. doi: 10.1103/PhysRevLett.117. 071801.

[24] R.; et al. Adhikari. A white paper on kev sterile neutrino dark matter. Journal of Cosmology and Astroparticle Physics, 2017, 01 2017. doi: 10.1088/1475-7516/2017/01/025.

[25] KatherineFreese.Statusofdarkmatterintheuniverse.InternationalJournalofModern Physics D, 03 2017. doi: 10.1142/S0218271817300129.

[26] Gerard Jungman; Marc Kamionkowski; Kim Griest. Supersymmetric dark matter. Phy- sics Reports, 267, 1996. doi: 10.1016/0370-1573(95)00058-5.

[27] Melissa van Beekveld, Wim Beenakker, Sascha Caron, Ruud Peeters, and Roberto Ruiz de Austri. This year's holiday present: Supersymmetry with Dark Matter is still natural. (1):1–6, 2016. URL http://arxiv.org/abs/1612.06333.

[28] Dieter Horns, Axel Lindner, Andrei Lobanov, and Andreas Ringwald. WISP Dark Matter eXperiment and Prospects for Broadband Dark Matter Searches in the 1eV– 10meV Mass Range. In Proceedings, 10th Patras Workshop on Axions, WIMPs and WISPs (AXION-WIMP 2014): Geneva, Switzerland, June 29-July 4, 2014, pa- ges 94–101, 2014. doi: 10.3204/DESY-PROC-2014-03/lobanov andrei. URL https: //inspirehep.net/record/1323442/files/arXiv:1410.6302.pdf.

[29] Baker et al. Improved experimental limit on the electric dipole moment of the neutron. Physical Review Letters, 97, 2006. doi: 10.1103/physrevlett.97.131801.

[30] S. Weinberg. Phys.Rev.Lett., 40(223), 1978.

[31] F. Wilczek. Phys.Rev.Lett., 40(279), 1978.

[32] R. Peccei and H. R. Quinn. Phys.Rev.Lett., 38(1440), 1977.

[33] A. D. Linde. Phys. Lett. B, 259(38-47), 1991.

[34] R. Corliss. Searching for a dark photon with darklight. Nuclear Instruments and Methods in Physics Research Section A: Accelerators, Spectrometers, Detectors and Asso- ciated Equipment, 7 2016. doi: 10.1016/j.nima.2016.07.053.

[35] C. Kelso, Halo simulations with baryons and direct detection of dark matter, in UCLA Dark Matter, 2016.

[36] J. I. Read, The Local Dark Matter Density, J. Phys., vol. G41, p. 063101, 2014.

[37] D. Tucker-Smith and N. Weiner, Inelastic dark matter, Phys. Rev., vol. D64, p. 043502, 2001.

[38] B. Montes, Analysis of the first underground run and background studies of the Argon Dark Matter, Ph.D. dissertation, UCM-CIEMAT, 2016.

[39] Laura Baudis. Direct dark matter detection: The next decade. Physics of the Dark Universe, 1, 11 2012. doi: 10.1016/j.dark.2012.10.006.

[40] David G. Cerdeno and Anne M. Green. Direct detection of WIMPs. 2010.

[41] David G. Cerdeño. Detection and identification of dark matter. International Journal of Modern Physics Conference Series, 01, 01 2011. doi: 10.1142/ s2010194511000134.

[42] Sigl G. Klasen, M.; Pohl. Indirect and direct search for dark matter. Progress in Particle and Nuclear Physics, 7 2015. doi: 10.1016/j.ppnp.2015.07.001.

[43] Academy of Sciences of the Institute of Bologna, editor. 30 Years of Bubble Chamber Physics Trent' Anni di Camere a Bolle, 2003.

[44] Frederick Seitz. On the theory of the bubble chamber. Physics of Fluids, 1, 1958. doi: 10.1063/1.1724333.

[45] Gibbs G.W. Collected works. Thermodynamics, volume Volume 1. Longmans, 1928. ISBN 146-149-154-1.

[46] Drew Anthony Fustin. First Dark Matter Results from the COUPP4 kg Bubble Chamber at a Deep Underground Site. PhD thesis, The University of Chicago, Chicago, Illinois, 3 2012.

[47] L. Bond; J.I. Collar; J. Ely; M. Flake; J. Hall; D. Jordan; D. Nakazawa; A. Raskin; A. Sonnenschein; K.O. Sullivan. Development of bubble chambers with sensitivity to wimps. New Astronomy Reviews, 49, 2005. doi: 10.1016/j.newar.2005.01.043.

[48] Mathieu Laurin. Recherche de la matiere sombre a l'aide de de tecteurs a' liquides surchauffe s dans le cadre de l'expe rience PICO/Picasso. PhD thesis, Universite de Montre al, Montreal, Quebec, 03 2016.

[49] C. Amole et al. PICO Collaboration. Dark matter search results from the pico-2l c3 f8 bubble chamber. Physical Review Letters, 114, 6 2015. doi: 10.1103/PhysRevLett.114. 231302.

[50] Behnke et al COUPP4 Collaboration. bubble chamber operated in a deep underground site. Physical Review D, 86, 9 2012. doi: 10.1103/PhysRevD.86.052001.

[51] V.A. Kudryavtsev. Background studies for dark matter experiments. Nuclear Physics B - Proceedings Supplements, 173, 2007. doi: 10.1016/j.nuclphysbps.2007.08.042.

[52] Ian T Lawson. Radon Levels in the SNOLAB Underground Laboratory 1 Radon Levels in the Underground SNO + Control Room. pages 1–41, 2016.

[53] Thomas K. Gaisser. Cosmic Rays and Particle Physics. Cambridge University Press, 1990. ISBN 0521339316,9780521339315,0521326672,9780521326674.

[54] A. Mei, D.-M.; Hime. Muon-induced background study for underground laboratories. Physical Review D, 73, 3 2006. doi: 10.1103/PhysRevD.73.053004.

[55] Yu-Cheng; et al. Wu. Measurement of cosmic ray flux in the china jinping underground laboratory. Chinese Physics C, 37, 08 2013. doi: 10.1088/1674-1137/37/8/086001.

[56] F. F. Khalchukov; et al. Hadrons and other secondaries generated by cosmic-ray muons underground. Il Nuovo Cimento C (Springer), 18, 09-10 1995. doi: 10.1007/bf02506782.

[57] F. Aubin et al PICASSO Collaboration. Discrimination of nuclear recoils from alpha particles with superheated liquids. 2008. doi: 10.1088/1367-2630/10/10/103017.

[58] A. Gutlein; et al. Solar and atmospheric neutrinos: Background sources for the direct dark matter searches. Astroparticle Physics, 34, 2010. doi: 10.1016/j.astropartphys. 2010.06.002.

[59] W.J. Bolte et al others. Development of bubble chambers with enhanced stability and sensitivity to low-energy nuclear recoils. Nuclear Instruments and Methods in Physics Research Section A: Accelerators, Spectrometers, Detectors and Associated Equipment, 577, 2007. doi: 10.1016/j.nima.2007.04.149.

[60] Alan Edward Robinson. Dark Matter Limits from a 2L C3F8 Filled Bubble Chamber. PhD thesis, The University of Chicago, Chicago, Illinois, 12 2015.

[61] Montecarlo simulation basics. URLhttps://www.vertex42.com/ExcelArticles/mc/MonteCarloSimulation.html.

[62] Geant4 Collaboration. Geant4—a simulation toolkit. Nuclear Instruments and Methods in Physics Research Section A: Accelerators, Spectrometers, Detectors and Associated Equipment, 506, 2003. doi: 10.1016/s0168-9002(03)01368-8.

[63] Rebecca K. Leane. Dark matter theory and new searches. CAASTRO-CoEOO Works- hop, 2017. URL http://www.caastro.org/files/58/2227658639/rkleane$_c$oepp$_c$aastro.pdf.$IX, 12S.WesterdaleandP.D$ $BackgroundExperiments,"$2017.

[64] *Compute Canada webpage: https://www.computecanada.ca*